GPR37L1 CONTROLS MATURATION AND ORGANIZATION OF CORTICAL ASTROCYTES DURING DEVELOPMENT

TrangKimberly Thu Nguyen[1,&], **Chad R. Camp**[1], **Juleva K. Doan**[1], **Stephen F. Traynelis**[1], **Steven A. Sloan**[2], **Randy A. Hall**[1,*]

[1]Emory University School of Medicine, Department of Pharmacology and Chemical Biology

[2]Emory University School of Medicine, Department of Human Genetics

Abstract

Astrocyte maturation is crucial to proper brain development and function. This maturation process includes the ramification of astrocytic morphology and the establishment of astrocytic domains. While this process has been well-studied, the mechanisms by which astrocyte maturation is initiated are not well understood. GPR37L1 is an astrocyte-specific G protein-coupled receptor (GPCR) that is predominantly expressed in mature astrocytes and has been linked to the modulation of seizure susceptibility in both humans and mice. To investigate the role of GPR37L1 in astrocyte biology, RNA-seq analyses were performed on astrocytes immunopanned from P7 *Gpr37L1*^{−/−} knockout (L1KO) mouse cortex and compared to those from wild-type (WT) mouse cortex. These RNA-seq studies revealed that pathways involved in central nervous system development were altered and that L1KO cortical astrocytes express lower amounts of mature astrocytic genes compared to WT astrocytes. Immunohistochemical studies of astrocytes from L1KO mouse brain revealed that these astrocytes exhibit overall shorter total process length, and are also less complex and spaced further apart from each other in the mouse cortex. This work sheds light on how GPR37L1 regulates cellular processes involved in the control of astrocyte biology and maturation.

TABLE OF CONTENTS

Main points:

RNA-seq analyses of astrocytes immunopanned from GPR37L1-knockout mouse cortex revealed alterations in pathways involved in brain development and genes involved in astrocytic maturation. Loss of GPR37L1 also leads to deficits in astrocyte morphological complexity and tiling in the mouse cortex.

Graphical Abstract

---

[*]Corresponding author <u>Address for correspondence:</u> Randy A. Hall, Department of Pharmacology and Chemical Biology, Rollins Research Center, room 5113, Emory University School of Medicine, Atlanta, GA, 30345. Phone: 404-727-3699. rhall3@emory.edu.
[&]Current address: Departments of Physiology and Neurobiology, University of California at Los Angeles, Los Angeles, CA
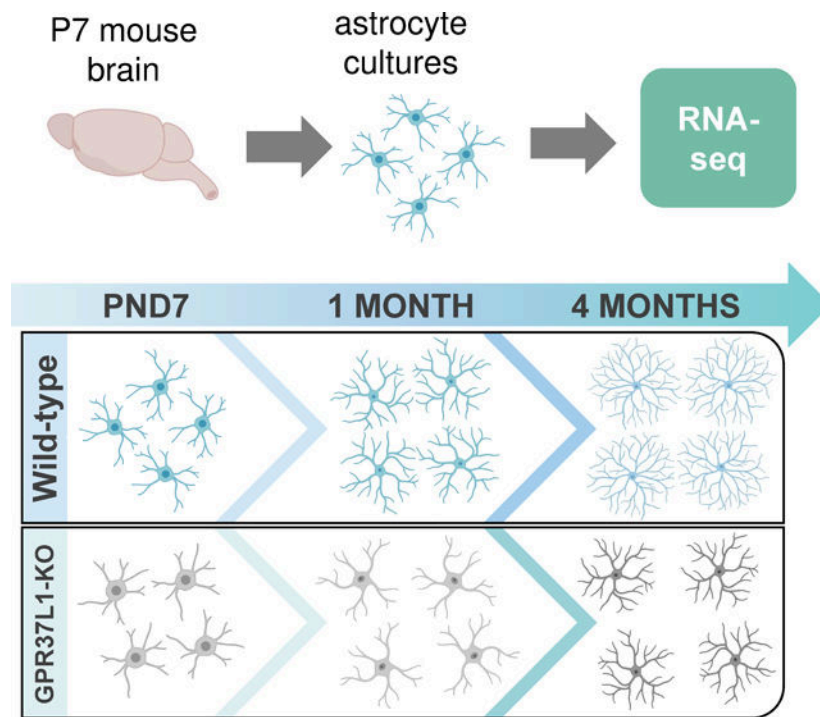
INTRODUCTION

Astrocytes are intimately involved in the normal health and function of the brain, including regulation of extracellular neurotransmitters, ions, and water, response to oxidative stress, formation of the blood-brain barrier, shaping of synapses, and determination of the fate of neural precursor cells (Liddelow & Barres, 2017; Vasile, Dossi, & Rouach, 2017; B. Zhou, Zuo, & Jiang, 2019). In order to perform these vital functions, astrocyte maturation must occur normally. The process of astrocyte maturation includes morphological changes where astrocytic processes ramify and become more spongiform as well as the activity-dependent establishment of astrocytic domains through contact-spacing or tiling in some brain regions such as the cortex (Bernardinelli et al., 2014; Bushong, Martone, & Ellisman, 2004; Bushong, Martone, Jones, & Ellisman, 2002; Hirrlinger, Hulsmann, & Kirchhoff, 2004; Li et al., 2019). Consequently, dysfunction in these processes during astrocytic maturation and development has been associated with a number of neurodevelopmental diseases and disorders, including Rett syndrome, Fragile X syndrome, epilepsy, and Alexander's disease (Molofsky et al., 2012; Quinlan, Brenner, Goldman, & Messing, 2007; Visanji et al., 2012). Specifically, loss of ramification and deficits in tiling have been characterized in mouse models of epilepsy (Arisi et al., 2011; Oberheim et al., 2009) and Fragile X Syndrome (Hagerman & Stafstrom, 2009), further suggesting the important role of astrocytic maturation in brain disorders and diseases. While much is known about how

astrocytes differentiate and mature, the mechanisms by which astrocyte maturation is initiated are still unclear.

GPR37L1 is an astrocyte-specific G protein-coupled receptor (GPCR) that has previously been implicated in epilepsy and seizure susceptibility via genetic studies (Dershem et al., 2019; Giddens et al., 2017). While little is known about the function of GPR37L1 in the brain, several datasets show that GPR37L1 is expressed predominantly in mature astrocytes, with expression in both mice and humans beginning in the first postnatal week (Cahoy et al., 2008; Clarke et al., 2018, Zhang et al., 2014, Zhang et al., 2016). This pattern of expression suggests that GPR37L1 may be involved in the maturation and/or development of astrocytes. While we previously showed that loss of GPR37L1 and the closely related receptor GPR37, which is predominantly expressed in oligodendrocytes, in adult mice leads to an altered global proteome in the mouse brain (Nguyen et al., 2020), the role of GPR37L1 specifically in astrocytes during development in the cortex was explored in the studies described below via RNA-seq and imaging analyses of astrocytes derived from mice lacking GPR37L1.

MATERIALS AND METHODS

Animals

GPR37L1 knockout mice (Gpr37L1$^{-/-}$) were obtained from the NIH Mutant Mouse Regional Resource Centers (strain Gpr37l1tm1Lex, stock number 011709-UCD), and genetic deletion of GPR37L1 was confirmed by DNA sequencing. C57BL/6J mice were used for wild-type experiments and all mice were maintained on a C57BL/6J background. Mice were housed on a 12-hour light/dark cycle with food and water ad libitum. All experiments were performed in accordance with the guidelines of the Institutional Animal Care and Use Committee (IACUC) of Emory University.

Immunopanned primary cortical astrocytes

Preparation of plates, dissection of mouse brains, and single-cell suspension
—Primary astrocytes were immunopanned from mouse cortex as previously described (Foo, 2013; Foo et al., 2011; Zhang et al., 2016). At least one day prior to immunopanning, 15cm petri dishes were prepared by incubating 60μL of the appropriate secondary antibody (corresponding with the primary antibodies that were used) in 25mL of 50mM Tris-HCl (pH 9.5) overnight at 4°C, making sure solution was covering the entirety of the dish's surface. On the day of immunopanning, the secondary antibody solution was removed from the prepared petri dishes and the dishes washed gently 3x with 1X Dulbecco's phosphate-buffered saline (DPBS). The appropriate primary antibody was then added to each plate in 12mL of 0.2% BSA/DNase solution (in 1X DPBS) and allowed to incubate at room temperature. Mouse brains were then extracted, cortices dissected out under a microscope, and meninges removed. For each genotype, 4–5 pup brains were pooled. Dissected cortices were placed in a 6cm petri dish (max of 5 cortices per dish) and cut into small pieces using a scalpel. Enzyme stock solution (0.46% D(+)-glucose, 0.5mM NaHCO$_3$, 100u of papain, 0.2mg/mL L-cysteine, 0.5mM EDTA in 1x Earl's Balanced Salt Solution) was equilibrated by bubbling CO$_2$ into the solution, and 10mL of equilibrated enzyme stock solution was added to each 6cm petri dish. Additionally, 50μL of 0.4% DNase was added and swirled into

each petri dish. Dishes were placed on a heater at 34°C with CO_2 gently bubbling onto the cortex and enzyme mixture and incubated for 45 minutes to allow digestion of the tissue. After digestion, the tissue mixture was transferred to 50mL conical tubes and the tissue was allowed to settle at the bottom of the tube. Supernatant was then carefully aspirated and tissue was washed by adding 4.5mL of low ovomucoid inhibitor solution (low ovomucoid stock solution final concentration: 8.5μM BSA, 20μM trypsin inhibitor (ovomucoid source, Worthington #LS003089) sterile filtered in DPBS (pH 7.4) in inhibitor stock solution: 0.46% D(+)-glucose, 26mM $NaHCO_3$ in 1X Earl's Balanced Salt Solution). Tissue was allowed to settle, supernatant was aspirated, and tissue was washed 2x. Low ovomucoid inhibitor solution (4mL) was then added to the washed tissue and tissue was gently triturated to break up the tissue. The cloudy single-cell solution was then transferred to a new 50 mL conical tube containing 4mL of low ovomucoid inhibitor solution. Trituration was repeated until most of the tissue chunks were gone. A layer of 12mL of high ovomucoid inhibitor solution (high ovomucoid stock solution final concentration: 21.2μM BSA, 50μM trypsin inhibitor (ovomucoid source) sterile filtered in 1X DPBS (pH 7.4) in inhibitor stock solution: 0.46% D(+)-glucose, 26mM $NaHCO_3$ in 1X Earl's Balanced Salt Solution) was carefully pipetted as a layer under the single-cell suspension. Cells were then centrifuged down through the high ovomucoid inhibitor solution at 300g for 5 minutes at room temperature. The supernatant was then aspirated and the cell pellet was resuspended in 3mL of panning buffer (0.02% BSA/DNase in 1X DPBS), and then the volume was brought up to 9mL with additional panning buffer. Finally, cells were filtered through a 0.4μM strainer to remove clumps.

Immunopanning—Before adding cells to each antibody-coated petri dish, antibody solution was removed and dishes were carefully washed 3x with 1X DPBS. Cells were added to the first dish and allowed to sit for 5 minutes, swirled, and then allowed to sit for another 5 minutes. The cell solution was then transferred to the second dish and allowed to sit for 5 minutes, swirled, and allowed to sit for another 5 minutes. This process was repeated until the final dish, which was specific for astrocytes. The order of plates to sequentially deplete specific cell types was as follows:

Plate #	Target cell type	Secondary antibody	Primary antibody
1	Microglia/macrophages	Anti-rat (60μL)	CD-45 (10μL, BD Biosciences 550539)
2	Oligodendrocyte precursor cells	Anti-rat (60μL)	PDGFRα (15μL, Thermo 14-1401-82)
3	Oligodendrocyte precursor cells	Anti-rat (60μL)	PDGFRα (15μL, Thermo 14-1401-82)
4	Neurons	Anti-rat (60μL)	Thy1.2 (10μL, Thermo 14-0902-82)
5	Astrocytes	Anti-mouse (60μL)	HepaCAM (15μL, R&D Systems MAB4108)

Culturing of immunopanned cortical astrocytes

Following incubation of cells in the final dish (HepaCAM), the remaining single cell mixture was aspirated off the dish and the dish was gently washed 3x with 1X DPBS. To lift immunopanned astrocytes off of the dish, 10 mL of trypsin was added to the dish, swirled, and cells were incubated at 37°C for 5 minutes. The dish was then banged on a

hard surface to lift cells off of plate and 10 mL of 30% fetal calf serum (FCS) was added to neutralize the trypsin. FCS was added only for the duration of the 5-minute spin. Cells were collected into a conical tube, counted, and then spun down at 300g for 5 minutes at room temperature. Cells were resuspended in serum-free astrocyte growth media (100 units/mL penicillin, 100μg/mL streptomycin, 1mM sodium pyruvate, 1% GlutaMAX, 1% Sato, 5μg/mL N-acetyl-L-cysteine (NAC), in 1:1 Neurobasal A and Dulbecco's Modified Eagle Medium (DMEM) and supplemented with fresh HBEGF (5ng/mL) each time media was made). Astrocytes were then plated onto poly-D-lysine-coated slides and plated at a density of 30,000 cells per well for 8-chamber slides and 25,000 cells per well for 6-well plates. Astrocyte growth medium was changed every 3 days.

Treatment of immunopanned cortical astrocytes and preparation of samples for RNA-seq analyses

Acutely-purified cortical astrocytes—For acutely-purified astrocytes used for RNA-seq analyses, following incubation of cells in the final dish (HepaCAM), the remaining cells were aspirated and the dish was washed gently 3x with 1X DPBS. To collect immunopanned cells for RNA isolation, 500 μL of TRIzol were added to the plate and cells were scraped and collected into Eppendorf tubes. RNA was then isolated according to the manufacturer's protocol. RNA samples were submitted to Novogene for RNA-seq analyses (NovaSeq 6000 PE150, polyA enrichment), including library preparation.

One-week cultured immunopanned cortical astrocytes +/– FBS—For immunopanned astrocytes that were cultured in vitro +/– fetal bovine serum (FBS), astrocytes were plated in 6-well plates (25,000 cells per well) and treated with 15% FBS every other day for 1 week. Following one week in culture, astrocytes were then collected in 500 μL TRIzol and RNA isolated according to the manufacturer's protocol. RNA samples were then submitted to Genewiz for RNA-seq analyses (Illumina HiSeq 2×150 bp sequencing, RNA with polyA selection, single index), including library preparation.

RNA-Seq data analyses

Raw read files were uploaded to Galaxy and data were analyzed via the public server at usegalaxy.com (Afgan et al., 2018). All steps were performed using the default settings unless otherwise noted. Raw read files were first trimmed with TrimGalore using the default settings to trim off adapters. Simultaneously, quality checks were done on raw reads as well as trimmed reads to ensure reads were valid. Following quality check and trimming, reads were then mapped to the mouse genome via RNA STAR (Dobin et al., 2013). Following alignment to the mouse genome (mm10), counts were quantified via featureCounts in order to measure the gene expression in our RNA-seq analyses (Liao, Smyth, & Shi, 2014). Differential expression of genes between different conditions was then determined by using DESeq2 (Love, Huber, & Anders, 2014). The resulting differential expression analyses were then run through GO ontological pathway analysis (Sherman et al., 2022).

Immunocytochemistry of immunopanned cells

Cells plated on coverslips were gently washed once with 1X DPBS and then incubated in 4% paraformaldehyde (PFA) for 10 minutes while shaking at room temperature. After

removal of the PFA, cells were then incubated in ice-cold methanol for 5 minutes while shaking gently at room temperature. Cells were washed once with 1X DPBS and incubated in blocking/permeabilization buffer (5% bovine serum albumin (BSA) and 0.5% Triton X-100 in 1X DPBS) for 1 hour while shaking gently at room temperature. After removing the blocking/permeabilization buffer, coverslips were then incubated with antibody diluted in antibody dilution buffer (1% BSA and 0.1% Triton X-100 in 1X DPBS) overnight at 4°C while shaking gently. Coverslips were washed three times with 1X DPBS for 5 minutes each while shaking gently at room temperature, and then incubated with secondary antibody diluted in antibody dilution buffer in the dark for 1 hour while shaking gently at room temperature. Coverslips were washed three times with 1X DPBS for five minutes each and then once with ddH$_2$O. Coverslips were mounted with Prolong Diamond Antifade mounting medium containing DAPI. Cells were imaged via confocal microscopy and images were analyzed via ImageJ and NeuronJ. All images were blinded prior to quantification and analysis.

Immunohistochemistry of free-floating brain sections

Whole mouse brain was dissected at various ages and fixed in 4% paraformaldehyde (PFA) for 24 hours at 4°C. Brains were then transferred to a 30% sucrose solution (in PBS) for 24 hours at 4°C. Coronal brain sections (40 μm) were then cut from the cerebellum and cortex and stored in cryoprotectant (30% ethylene glycol, 15% sucrose, 0.05% sodium azide, in TBS) at −20°C until staining and mounting. Brain sections were washed 3x with 1X DPBS for 5 minutes each. Sections were then permeabilized in 1% H$_2$O$_2$ solution for 15 minutes at room temperature. Sections were washed 3x in 1X DPBS for 5 minutes each and then incubated in pre-block solution (0.3% Triton X-100, 15% normal goat serum, 2.5% Brij 35, in 1M Tris-HCl, pH 7.5) for 1 hour at 4°C. Sections were then incubated in primary antibody diluted in Tris-Brij solution (2.5% Brij 35 in 1M Tris-HCl, pH 75) overnight at 4°C. The next day, sections were washed 3x in Tris-Brij solution for 5 minutes each and then incubated with fluorescently labeled secondary antibody in Tris-Brij solution for 1 hour at 37°C in the dark. Sections were then washed 3x with Tris-Brij solution for 5 minutes each and sections were mounted with mounting media onto glass slides and cover slipped. Slides were allowed to dry overnight in the dark before imaging via confocal microscopy. Images are analyzed with Fiji (ImageJ) as previously described (Schindelin et al., 2012; Varvel et al., 2012). All images were blinded prior to image quantification and analysis. The timepoints of 1 week, 1 month, and 4 months were chosen due to their significance in astrocyte maturation: at 1 week, astrocytes are immature and just beginning to mature and differentiate; at 1 month, astrocytes are completing maturation and differentiation; and at 4 months, astrocytes are mature and fully differentiated (Zarei-Kheirabadi, Vaccaro, Rahimi-Movaghar, Kiani, & Baharvand, 2020).

Western blot analysis

Brain samples were made into Western blot samples and samples were run on 4–20% Tris-glycine gels and then transferred to nitrocellulose membranes. Membranes were incubated in 5% non-fat milk to block for 1 hour at room temperature while shaking and then incubated in diluted primary antibody overnight at 4°C while shaking. Membranes were then washed and incubated with diluted secondary antibody at room temperature while shaking

and then washed. Membranes were developed and imaged via the Licor Odyssey Western blot imaging system. Protein quantification was done via ImageJ.

Iontophoretic backfilling of cortical astrocytes

Astrocytes in the somatosensory cortex were backfilled as previously described (Moye, Diaz-Castro, Gangwani, & Khakh, 2019). All mice used were 6–8 weeks old with data obtained from both males and females. After an overdose of inhaled isoflurane, four GPR37L1$^{-/-}$ mice and four age-matched WT control mice were transcardially perfused using cold 1X phosphate buffered saline (PBS) to clear blood, then perfused with 4% paraformaldehyde (PFA) in PBS (pH 7.35) for 5–7 minutes. After perfusion, brains were incubated in 4% PFA in PBS for an additional 45 minutes before being sliced into 150 μm-thick coronal slices using a vibratome (Leica VT1200S). Brain slices were incubated in PBS at 4°C for no more than 48 hours. Sharp electrodes (tip resistance ~50 MΩ) were pulled on a horizontal electrode puller (Sutter P1000) from thin-walled borosilicate glass (WPI) and backfilled with filtered 2% Lucifer Yellow lithium salt (Thermo L453) in 5mM KCl using gravity to help assist complete tip filling. Slices were placed in a dish of 1X PBS and astrocytes were visualized using an upright Olympus BX50W microscope with IR-DIC optics coupled to a Dage IR-2000 camera. Astrocytes in the somatosensory cortex were chosen based on their stereotypical oval shape and small soma size. To ensure electrode tips were not clogged before impaling, test pulses consisting of injecting 1nA of current for 1 second every 2 seconds were administered using a Multiclamp 700B (Molecular Devices), digitized at 20kHz using an Digidata 1440a (Molecular Devices), and controlled by pClamp 10.6 software (Molecular Devices). To visualize Lucifer Yellow injection from the tip, a WGFP filter cube set (Thorlabs, TLV-U-MF2-WGFP) was excited via 455nm collimated LED light source (Thorlabs, M455L4-C1) to ensure the electrode was not clogged before impaling. Immediately after impaling, a few test pulses were given and cell morphology was checked to ensure an astrocyte had been chosen. After confirming cell identity, iontophoretic backfilling via test pulses described above continued for 15 minutes before the electrode tip was slowly withdrawn from the cell. After filling, slices were incubated in 4% PFA in PBS overnight. After incubation, slices were washed 3X in PBS for 10 minutes each before being mounted on SuperFrost slides. After slices dried in the dark overnight, they were coverslipped using #1.5 coverslips and mounted with ProLong Gold mounting media.

All images were acquired using a Nikon A1R HD25 line-scanning confocal microscope using NIS Elements software. A 455nm argon laser line coupled to a GaAsP PMT detector was used to excite and collect fluorescent data. All images were captured as a series of z-stacks using a piezo motor z-controller with software set to acquire data in 1024×1024 pixel format at a 1/8th frame rate dwell time. All images were captured using an Apo TIRF 60× 1.49 NA objective plus 3X additional zoom, with images consisting of 55–85 stacks with a z-stack distance of (0.3μm) and a pinhole size of 30.4μm. All images were analyzed in Imaris 9.5 (Bitplane).

Quantification methods of confocal images

Distance mapping—Distances between astrocytes were measured via MorphoLibJ and Fiji (ImageJ), as previously described (Legland, Arganda-Carreras, & Andrey, 2016; Varvel

et al., 2012). Confocal stacks were obtained from 40 μm-thick coronal mouse brain sections and stained according to the immunohistochemistry protocol outlined above. Images were taken with the Leica SP8 inverted confocal microscope. For image analysis, 10 stacks were taken for each area of interest in the cortex and 2–4 stacks of in-focus images were compressed into one image for analysis. Cell surfaces were reconstructed in Fiji and then a distance map was calculated via Chamfer distance map (MorphoLibJ), which computes the distance of each pixel (in space) from the nearest cell surface.

Quantification of total process length and cell numbers—Astrocyte process length was manually measured using NeuronJ (ImageJ) tracer. Primary branches were defined as any astrocyte process that extended from the astrocyte soma. Cell counter was used to manually count the number of astrocytes per field.

Sholl analysis—Sholl analysis was done in Fiji (ImageJ) using the "Neuroanatomy" plugin. Images of astrocytes taken at 40x were used to perform Sholl analysis as previously described (Binley, Ng, Tribble, Song, & Morgan, 2014; Sethi et al., 2021; Sholl, 1953). Images were thresholded to obtain a binary image with background removed and individual astrocytes were analyzed. Regions of interest (ROIs) were determined as the soma of an astrocyte and concentric circles were drawn around the soma in 10 μm steps. The number of intersections per radius (distance from soma) was plotted to obtain Sholl analysis plots for each astrocyte.

Statistical analyses—All statistical analyses were performed in Prism 6 (GraphPad Software) as well as all graphical representations. Statistical significance was defined as a p value $\leq$ 0.05. All analyses were performed in a blinded manner.

Antibodies used

GFAP (Abcam, catalog #: ab7260) 1:1000 for ICC and IHC, 1:5000 for Western blot; aquaporin-4 (Abcam, catalog #: ab125049) 1:400 for ICC

RESULTS

Validation of the purity of immunopanned cortical astrocytes

The immunopanning methodology is an effective way to purify and culture different cell types from brain tissue of different age points, including astrocytes at more than 98% purity (Foo et al., 2011). Previous methods to purify and culture astrocytes required the use of rodent brains before the age of P5, as astrocytes from mice past the age of P5 did not survive the protocol (McCarthy & de Vellis, 1980; Morrison & de Vellis, 1981). We utilized the immunopanning method to obtain pure cultures of postnatal day 7 (P7) cortical astrocytes from our mice to conduct RNA-seq analysis and chose P7 as our timepoint since that is the age at which GPR37L1 is first expressed in high levels in the mouse brain (Cahoy et al., 2008). Additionally, we expected fewer significant gene changes at this timepoint since high GPR37L1 expression begins around this time and any gene changes that occur at this timepoint may be reflective of more immediate changes as a direct result of loss of

GPR37L1 rather than downstream effects due to loss or dysfunction of other genes and/or proteins. The experimental conditions are outlined in the schematic in Figure 1A.

Because oligodendrocyte precursor cells (OPCs) share a cell lineage with astrocytes (Behar, 2001; Nishiyama, Komitova, Suzuki, & Zhu, 2009; Nishiyama, Suzuki, & Zhu, 2014; Nishiyama, Watanabe, Yang, & Bu, 2002) and are numerous in the rodent brain at P7 (Tiane et al., 2019; J. Zhou et al., 2019), the purity of our immunopanned astrocytes was assessed by looking at FPKM (Fragments Per Kilobase of transcript per Million mapped reads) values of selected cell-specific gene markers in WT astrocytes. Our results showed that immunopanned cortical astrocytes submitted for RNA-seq analysis were highly enriched in astrocytic genes, with depletion of neuronal, mature oligodendrocytic, microglial, and endothelial genes. The key astrocytic markers that were enriched included glial fibrillary acidic protein (Gfap), Aldh1l1, Slc1a2, and Aqp4 (Flugge, Araya-Callis, Stadelmann-Nessler, & Fuchs, 2014; Zhang et al., 2014; Zhang et al., 2016) (Figure 1B). We did observe low expression of several OPC-specific markers within our purified samples, such as platelet-derived growth factor alpha (PDGFRα). However, OPCs are known to also express a low level of HepaCAM, which was used to specifically immunopan out astrocytes, as described in the Methods section (Zhang et al., 2014). Additionally, Gpr37l1 has no detectable expression in OPCs based on the databases cited above. Overall, these data demonstrate the high enrichment of astrocytes in the samples prepared for the RNA-seq analyses, with only a very low level of contamination from other cell types.

RNA-seq of acutely purified astrocytes from L1KO and WT mice reveal gene and pathway changes related to brain development

In order to assess what gene changes may be occurring specifically in astrocytes due the loss of GPR37L1, RNA-seq analysis was performed on GPR37L1 homozygous knockout (L1KO) vs. WT astrocytes. Astrocytes were immunopanned from P7 L1KO and WT mouse cortex and immediately collected in TRIzol for RNA isolation. Samples were then submitted for RNA-seq and Differential Expression Analysis (DESeq2) was performed to obtain $\log_2$(Fold Change) values for gene changes between the two genotypes (n=4 for each genotype). An Excel file containing the FPKM values for gene expression for these individual samples is also included in the supplement (Supplemental Material S3). The RNA-seq analysis yielded over 24,000 gene hits. However, of the 24,000 genes, only 127 genes were found to be significantly upregulated and only 160 genes significantly downregulated based on a p value equal to or less than 0.05 (Supplemental Material S1). The top 50 most significantly downregulated and the top 50 most significantly upregulated genes are displayed in Tables 1 and 2. The appearance of GPR37L1 at the top of the list of downregulated proteins validates the fact that our L1KO astrocytes were indeed from knockout brains. The complete lists of upregulated and downregulated genes were then analyzed via GO enrichment analysis for gene ontologies ("biological process," "cellular component," and "molecular function") in order to identify which specific pathways may be affected by the knockout of GPR37L1 in astrocytes. Ontologies were sorted via gene count. GO analyses showed that loss of GPR37L1 led to the loss and gain of many important biological processes. These include proteolysis, cell adhesion, and oxidoreductase activity (Supplementary Figures S1A–I). Of note, however, were pathways involved in calcium

ion transport, central nervous system development, potassium ion transport, and neuron projection development (Supplementary Figure S1G). These ontological analyses suggest that major gene changes that occurred due to the loss of GPR37L1 in astrocytes were related to brain development as well as ion transport and homeostasis.

RNA-seq analyses of L1KO vs. WT immunopanned astrocytes reveal gene and pathway changes after 1 week in culture

While assessing the effect of loss of GPR37L1 on gene changes in acutely immunopanned astrocytes showed changes in pathways involved in brain development and ion transport, we were also interested in assessing how loss of GPR37L1 affects FBS-induced astrocyte reactivity, which can be done in culture. Studies in cultured astrocytes from WT vs. L1KO animals are relevant because they allow for the astrocytes to be treated with reagents of interest under controlled conditions prior to harvest in order to observe changes that occur due to specific manipulation of the astrocytes. Additionally, culture studies remove the potential confound of gene changes that may occur as a result of response to stimuli from other cell types in the brain. First, RNA-seq analysis was performed on immunopanned astrocytes from P7 L1KO and WT mice that were cultured for 1 week *in vitro* (n=2 for WT and n=3 for L1KO; one WT sample was removed as an outlier based on Principal Component Analysis). The top 50 most significantly downregulated genes and the top 50 most significantly upregulated genes in L1KO astrocytes compared to WT astrocytes are reported in Tables 3 and 4. An Excel file containing the FPKM values for gene expression for these individual samples is also included in the supplement (Supplemental Material S4). After a week in culture, P7 L1KO immunopanned astrocytes exhibited many more significant gene changes (versus WT immunopanned astrocytes) compared to L1KO astrocytes that were acutely immunopanned from the mouse brain (versus WT immunopanned astrocytes).

Of over 24,000 gene hits, 985 genes were found to be significantly downregulated and 1391 genes were found to be significantly upregulated in L1KO astrocytes that were cultured for a week compared to WT astrocytes that were cultured for a week (Supplemental material S2). These numbers differ compared to 127 and 160 significantly upregulated and downregulated genes found in acutely purified L1KO astrocytes compared to WT astrocytes, respectively. Genes of note that were significantly downregulated include LCN2 (−73.81%), KCNIP3 (−53.96%), ATP1A2 (−53.28%), NDRG2 (−52.35%), CPE (−52.20%), and KCJN10 (−50.70%). These genes were of interest because of their reported involvement in GO ontological pathways that were found to be changed in acutely immunopanned L1KO astrocytes compared to acutely immunopanned WT astrocytes and/or their reported association with a seizure/epilepsy phenotype (Hong, Jo, Lee, Kim, & Jung, 2003; Jiang, Li, Wu, Hao, & Feng, 2021; Mahata et al., 1993; Mir et al., 2019; Moya-Mendez et al., 2021; Reichold et al., 2010; Shin et al., 2021; Vetro et al., 2021; Yin et al., 2020; J. Zhou et al., 2020).

The lists of significantly downregulated or upregulated genes were analyzed via GO enrichment analysis to generate ontology graphs. Following induction of reactivity in culture, pathways and processes affected that were of note included signal transduction,

metabolism, nervous system development, brain development, and positive regulation of neuron projection development (Supplementary Figures S2A–I). Taken together, these ontological analyses suggest that significantly downregulated genes appear to be more involved in pathways involved in central nervous system development and ion transport activities whereas significantly upregulated genes appear to be more involved in GPCR activity, metabolic processes, and binding of different cellular components.

Loss of GPR37L1 leads to changes in expression of mature astrocytic genes but not fetal genes

It is known that GPR37L1 is highly expressed in mature astrocytes and that expression of GPR37L1 begins in the early post-natal period in mice (Cahoy et al., 2008; Zhang et al., 2014). Because ontological pathways related to brain and neuronal development were found to be represented by the most significantly down- and upregulated genes in the RNA-seq analyses, we looked at expression of specific fetal and mature astrocytic genes. Log_2(Fold Change) values of 100 fetal astrocytic genes and 100 mature astrocytic genes were evaluated for any significant changes between L1KO astrocytes versus WT astrocytes. These lists of fetal and mature astrocytic genes were curated and carefully validated in previously published studies (Sloan et al., 2017; Zhang et al., 2016). Evaluation revealed that fetal astrocytic genes were not significantly changed in L1KO versus WT acutely immunopanned astrocytes from P7 mice (Figure 2A). Only five genes were found to be significantly changed between L1KO versus WT astrocytes: GPR37L1 (not shown on graph), TNC, LIPG, CNR1, and RPPH1. Additionally, approximately half of fetal genes had log_2(Fold Change) values $1<$ with the other half having log_2(Fold Change) values >1, further suggesting that there was no skew of gene expression to being downregulated or upregulated. Heat map visualization of Z scores of individual samples for fetal astrocytic genes showed variability between samples (Figure 2B).

RNA-seq data was also assessed for expression of 100 mature astrocytic genes. Similar to fetal astrocytic genes, the majority of mature astrocytic genes were not significantly changed in L1KO astrocytes compared to WT acutely immunopanned astrocytes (Figure 2C). Five genes were found to be significantly changed in L1KO astrocytes compared to WT astrocytes: CYBRD1, ATP1A2, MRO, and KCNJ10. Interestingly, unlike fetal astrocytic genes, most mature astrocytic genes were downregulated, suggesting a deficit or delay in the activation of maturation genes due to the loss of GPR37L1. A heat map of Z scores was also generated for individual samples for mature astrocytic genes, which showed some variability between the different samples (Figure 2D). Due to this variability, most of the changes in fetal or mature astrocytic genes that were observed at P7 upon loss of GPR37L1 in the acutely immunopanned astrocytes were not found to be statistically significant.

Similar to the acutely immunopanned astrocytes, we also assessed whether fetal and mature astrocytic genes were changed in L1KO immunopanned astrocytes compared to WT immunopanned astrocytes after 1 week in culture. When looking at the list of 100 fetal astrocytic genes, only PTTG1 was significantly downregulated and EOMES and NPY were significantly upregulated (Figure 2E). The heatmap generated also shows that there were low levels of variability between the WT and L1KO astrocytes (Figure 2F). Interestingly

however, when we looked at the list of 100 mature astrocytic genes, we found that a strong majority of these genes were downregulated in L1KO vs. WT, with 27 of these downregulated genes achieving statistical significance and being reduced very substantially, by 40% or more (p value less than or equal to 0.05). These significantly-downregulated genes included key mature astrocytic markers such as ATP1A2, NDRG2, CPE, ALDOC, KCNJ10, FGF1, GLUL, AQP4, PTGDS, GPR37L1, and ALDH2. (Figure 2G). Conversely, no mature astrocytic genes were found to be significantly upregulated. A corresponding heat map revealed low within-group variability in the astrocyte samples (Figure 2H). Taken together, these data suggest that the loss of GPR37L1 contributes to the loss or delay of astrocytic maturation.

GPR37L1-knockout does not alter astrocyte reactivity

Because astrocytes are known to become "reactive" in response to different insults and disease contexts within the brain, we also assessed the expression of 38 reactive astrocytic genes, as described in work by Liddelow and colleagues (Liddelow et al., 2017). This list of reactive astrocytic genes is divided into categories representing 3 different subtypes of reactivity: inflammation-induced, stroke-induced, and pan-reactive (Liddelow et al., 2017; Escartin et al., 2019). These different subtypes of reactivity were characterized based on what induces the specific astrocytic reactive state as well as the corresponding astrocytic gene profile once in the reactive state. Inflammation-induced reactive astrocytes have been shown to secrete neurotoxins that lead to the death of neurons and stroke-induced reactive astrocytes have been shown to promote neuronal survival and tissue repair (Liddelow et al., 2017). It is important to note that this list of reactive astrocytic genes is not exhaustive or immutable, and often a subset of transcripts from all three categories can be upregulated or downregulated in different disease states (Escartin et al., 2019). Our RNA-seq analyses of acutely-purified astrocytes revealed that at baseline in the mouse brain, astrocytes are not significantly more or less reactive due to the loss of GPR37L1 across the three different subtypes of reactivity (Figure 3A). Additionally, heat map visualization of Z scores of the individual samples revealed high variability between the samples for reactive astrocytic genes (Figure 3B). These data suggest that loss of GRP37L1 in astrocytes does not inherently make astrocytes more reactive in the mouse brain at baseline.

In addition to these RNA-seq analyses of the acutely-immunopanned astrocytes, we also assessed expression of reactive astrocytic genes in the immunopanned astrocytes that were cultured for a week. Across the 3 subtypes of astrocytic reactivity, only 3 genes were significantly upregulated (B3GNT5) or downregulated (GFAP, VIM) (Figure 3C). A heat map showed that there was only slight variability in expression of reactive astrocyte genes across the individual samples (Figure 3D). Overall, these data suggest that neither loss of GPR37L1 nor culture conditions caused an increase in astrocyte reactivity in untreated cultures. However, we were additionally curious whether loss of GPR37L1 might affect the gene expression profile of astrocytes once already in the reactive state. Thus, pan-reactivity was induced in immunopanned and cultured astrocytes via treatment with 15% FBS as previously described (Cahoy et al., 2008; Codeluppi et al., 2011; Doyle et al., 2008; Foo et al., 2011; Prah et al., 2019). These astrocytes were collected at the same time as astrocytes that had not been treated with FBS for RNA-seq analysis. For these

analyses, each genotype of astrocyte sample that was treated with 15% FBS for 1 week was compared to its non-treated baseline control in order to normalize values for baseline gene expression (i.e., 15%-FBS-treated WT astrocyte gene expressions were normalized to non-treated WT astrocyte gene expressions via DESeq2 to get Log_2(Fold Change) values and the same was done for L1KO astrocytes). These values were then compared to each other to assess the level of reactive astrocyte gene expression between WT and L1KO astrocytes after 1 week in culture. The data revealed that, outside of a handful of genes that were different between L1KO and WT astrocytes, the majority of reactive astrocytic genes were not changed between the two genotypes after treatment with 15% FBS (Figure 3E). Additionally, the direction of gene changes mostly trended in the same direction for both genotypes with the majority of the reactive astrocytic genes being upregulated with some that were unchanged or downregulated. The upregulation of reactive astrocytic genes for all genotypes examined was consistent with previously published studies (Liddelow et al., 2017). The heat map for the reactive genes in the individual astrocyte samples showed that there was strong consistency in which genes are upregulated or downregulated when each genotype of astrocytes was treated with 15% FBS (Figure 3F). Interestingly, both L1KO and WT immunopanned astrocytes appeared to significantly upregulate stroke-induced and pan-reactive astrocytic genes while only a handful of inflammation-induced reactive astrocytic genes were upregulated by the FBS treatment.

Loss of GPR37L1 leads to decreased total process length in immunopanned astrocytes

The RNA-seq data described above suggest that GPR37L1 is involved in the maturation of astrocytes in the cortex. Part of the process of astrocytic maturation involves morphogenesis into a complex, ramified, and spongiform shape as well as establishment of spatial non-overlapping domains within the brain (Bushong et al., 2004; Bushong et al., 2002; Freeman, 2010; Li et al., 2019; Zarei-Kheirabadi et al., 2020). Thus, we investigated whether these characteristics of astrocyte maturation might be affected by the loss of GPR37L1 *in vitro* as well as in the mouse cortex. Cortical astrocytes were immunopanned from P7 L1KO and WT mouse brains, plated onto PDL-coated coverslips, fixed, and stained with GFAP, AQ4, and DAPI to visualize astrocytes. This *in vitro* assay is good for looking at morphological differences in the large, major branches of astrocytes. Various characteristics of astrocyte morphology were assessed and quantified to see if there were any differences between the L1KO vs. WT immunopanned astrocytes after 1 day in culture based on previously-reported methods of quantifying astrocyte morphology (Moye et al., 2019; SheikhBahaei et al., 2018). The properties that were quantified included number of primary branches, number of branch points, soma size (μm), and total process length (μm) (n=9 for WT, n=14 for L1KO). Soma size was determined by measuring the diameter of the astrocytic cell body and total process length was quantified by summing measurements of all processes that were labeled by GFAP staining. For branch quantifications, primary branches were defined as any branch originating from the astrocyte cell body, and the number of branch points was defined as any part of the astrocytic process where another process originated from an astrocytic branch. Soma size, number of primary branches, and number of branch points were not found to be significantly different between L1KO and WT immunopanned astrocytes (Figure 4C–E). However, when total process length was measured for each astrocyte, L1KO astrocytes exhibited significantly shorter total process length compared to WT astrocytes by almost 100

μm (Figure 4B, representative images in Figure 4A) (p=0.0299). This was not due to overall reduced expression of GFAP in L1KO mouse brains or astrocytes, as protein expression and mRNA expression levels of GFAP in L1KO animals were not found to differ (Figure 4F–H). Overall, these results suggest that GPR37L1 plays a role in the development of astrocytic processes and astrocyte morphology.

Loss of GPR37L1 leads to loss of astrocytic complexity at older timepoints in the mouse cortex

The aforementioned studies with immunopanned astrocytes revealed that L1KO astrocytes *in vitro* exhibit shorter total process length compared to WT astrocytes. These *in vitro* data suggest that the loss of GPR37L1 leads to decreased complexity in astrocytes, which may in turn be related to a deficit or delay in maturation. To determine if the same morphological abnormalities are observed in astrocytes *in vivo* in the native mouse cortex, brain sections from 1 week, 1 month, and 4-month-old L1KO vs. WT mice were stained with GFAP to visualize cortical astrocytes. Sholl analyses were then performed to determine if there were differences in astrocyte complexity between L1KO and WT astrocytes at these three different age points. Sholl analysis is normally used to describe the complexity of neurons but has also been used effectively to describe the complexity of glial cells such as astrocytes and microglia (Binley et al., 2014; Heindl et al., 2018; Kongsui, Beynon, Johnson, & Walker, 2014; Naskar & Chattarji, 2019; Sethi et al., 2021). At 1 week, L1KO cortical astrocytes were already found to be significantly less complex compared to WT astrocytes as indicated by a smaller number of intersections measured at 15 μm, 20 μm, and 25 μm from the astrocyte soma (Figure 5A). At 1 month of age, L1KO astrocytes continued to exhibit fewer numbers of intersections compared to WT astrocytes at further distances from the soma, although these differences did not achieve statistical significance according to the Sholl analyses (Figure 5B). However, the decreased complexity was again observed at 4 months of age, with the differences between L1KO and WT at this time point achieving clear statistical significance (Figure 5C).

Other morphological characteristics of the *in vivo* astrocytes were also quantified, including those that were previously quantified in the immunopanned astrocytes: total process length (Figure 5D), number of primary branches (Figure 5E), number of branch points (Figure 5F). Additionally, the numbers of astrocytes per 270 μm^2 field were also quantified (Figure 5G). Similar to the P7 immunopanned astrocytes, L1KO astrocytes in 1-week-old mice *in vivo* did not have significantly different numbers of primary branches or numbers of branch points. However, there was a significant difference in total process length between L1KO and WT astrocytes at 1 week (~60 μm). At 1 month of age, the difference in total process length was even more pronounced between L1KO and WT astrocytes (~150 μm) and the number of primary branches and number of branch points became significantly different as well. These deficits in total process length, number of primary branches, and number of branch points were still observed at the 4-month time point. However, the numbers of astrocytes, defined as GFAP-positive cells, quantified per 270μm^2 field did not differ between WT and L1KO brains at any timepoint investigated, suggesting that the differences observed in the images are due to the size and/or spacing of the astrocytes. Taken together, these data suggest that loss of GPR37L1 affects astrocyte morphogenesis

throughout development, with the complexity and total length of astrocytic processes being particularly affected.

GPR37L1 knockout leads to sparser astrocytic tiling in the mouse cortex

Another important aspect of astrocytic development *in vivo* is tiling, or the segregation of astrocytic processes into independent domains. This process is believed to be important for astrocyte function, in part because tiling is often perturbed in disease states (Cho, Muthukumar, Stork, Coutinho-Budd, & Freeman, 2018; Khurgel & Ivy, 1996; Lenzer-Fanara, Li, Salerni, Payen, & Croll, 2017; Oberheim et al., 2009; Tashiro, Goldberg, & Yuste, 2002). To assess whether GPR37L1 deletion exerts effects on astrocytic tiling in the mouse brain *in vivo*, distance mapping was done to calculate the distance between astrocytes in a given field. Cortical astrocytes near the periventricular zones in the cortex were imaged and analyzed (Buffo et al., 2008; Carlen et al., 2009). Distances were grouped into 5 bins representing the distance between astrocyte-negative pixels and the nearest astrocyte-positive pixel: 0–3 μm, 3–9 μm, 9–15 μm, 15–21 μm, and 21–30 μm. The number of measured distances in bins of shorter distances represents astrocytes that were closer to each other, whereas measurements in bins of longer distances mean that astrocytes were spaced further apart from each other. At 1 week of age, the spacing between WT and L1KO astrocytes was not significantly different, with the majority of measured distances being 0–3 μm and L1KO astrocytes having slightly more space between astrocytes with about 40,000 measured distances at 3–9 μm compared to WT astrocytes, which had fewer than 30,000 measured distances at 3–9 μm (Figure 6B, with representative images in Figure 6A). The number of measured distances in other ranges were similar and not significantly different between WT and L1KO.

When astrocytes in cortices from older mice were assessed, loss of GPR37L1 resulted in a pronounced effect on the amount of space between astrocytes. At the 1-month timepoint, for example, the majority of WT astrocyte surfaces were less than 3 μm (~234,000) from other astrocyte surfaces, with a smaller number of measured distances at 3–9 μm (~26,000). Similarly, a large portion of L1KO astrocyte surfaces were less than 3 μm (~188,000) from other astrocytes. However, a large number of astrocyte surfaces were also found 3–9 μm (~63,000) from other astrocytes compared to WT, with the numbers of distances in this range being significantly different between L1KO and WT (p<0.001). Astrocytes in the L1KO brains also exhibited a significantly higher number of measurements at 9–15 μm (~8,500) compared to astrocytes from WT mice (~1,400) (Figure 6C–D). At the 4-month timepoint, the differences in astrocyte tiling between WT and L1KO brains were even more pronounced., Notably, there was a dramatically larger number of astrocytes that were 3–9 μm away from other astrocytes in the L1KO mouse brains (~75,000) and also a much larger number of astrocytes that were 9–15 μm away (~13,000) from other astrocytes compared to astrocytes from the WT brains (~20,000 measurements at 3–9 μm and ~900 measurements at 9–15 μm for WT) (Figure 6E–F). These data suggest that at early age points where postnatal astrocyte maturation is just beginning, the loss of GPR37L1 does not significantly affect astrocyte tiling. However, at later stages of development (1 month and 4 months), loss of GPR37L1 exerts striking effects on astrocyte tiling, resulting in astrocytes that are spaced much further apart from each other.

Given the dramatic differences in astrocyte tiling that were observed between L1KO and WT brains, we next sought to determine whether these differences in tiling might be accounted for by differences in astrocyte size or volume. Due to the fact that GFAP is not expressed in the fine distal processes of astrocytes, immunofluorescent staining with GFAP cannot reveal the true size and volume of astrocytes (Connor & Berkowitz, 1985; Kalman, 2002). Thus, to assess whether loss of GPR37L1 affects total astrocyte size and volume, somatosensory cortical astrocytes from 6–8-week-old WT and L1KO mice were backfilled with Lucifer Yellow, as previously described (Moye et al., 2019), and cell volume, soma volume, number of major branches, and number of minor branches were quantified (Figure 7). Quantification of soma volume and total cell volume revealed that while there was a trend of L1KO astrocytes having overall smaller cell and soma volumes compared to WT astrocytes, but there were no significant differences. The same was true of the number of minor and major branches calculated. These results suggest that the sparser astrocytic tiling observed in the L1KO mouse brain is not due to differences in cell volume or size of the fine distal processes of the astrocytes.

DISCUSSION

Our immunohistochemical studies combined with our RNA-seq analyses provide evidence for a key role of GPR37L1 in astrocyte maturation. GO ontological analyses on RNA-seq data from L1KO astrocytes revealed alterations in pathways involved in central nervous system development and brain development. The inclusion of pathways involved in CNS development is particularly intriguing since astrocytes are known to be heavily involved in processes such as guiding neurons to the correct place in the developing brain (Malatesta, Appolloni, & Calzolari, 2008; Meyerink, Tiwari, & Pilaz, 2020; Turrero Garcia & Harwell, 2017; Xu et al., 2015) and pruning neuronal synapses (Chung, Allen, & Eroglu, 2015; Chung et al., 2013; Lee & Chung, 2019). Our RNA-seq analyses further suggest that GPR37L1 regulates expression of astrocytic maturation genes. In particular, our findings suggest that GPR37L1 exerts control over astrocytic tiling and astrocytic process maturation, two processes that are essential to the proper functioning of astrocytes in the brain. At 1 week of age, protoplasmic hippocampal astrocytes have been shown to exhibit more ovoid soma shapes and fine processes that are predominantly stringy and filamentous in nature; by postnatal day 14, astrocytic processes have been shown to exhibit greater ramification, and, by postnatal day 21 and beyond, astrocytes develop spongiform and extremely fine processes that are characteristic of mature astrocytes (Bushong et al., 2004; Bushong et al., 2002). Astrocytic domains have also been shown to start forming as early as postnatal day 7, with boundaries being clearly defined by 4 weeks of age (Bushong et al., 2004). It is purported that astrocytic morphology and tiling are determined by "contact-spacing" where astrocytes maintain contact with neighboring astrocytes through gap junctions in their distal processes, tightly regulating their own microdomains (Chang Ling & Stone, 1991; Dreher, Tout, & Stone, 1994; Tout, Dreher, Chan-Ling, & Stone, 1993).

While the exact functional significance of astrocytic tiling is still unclear, loss of tiling and reduced morphological complexity are seen in certain disease and injury states. Relevant to the disease phenotype associated with mutations in GPR37L1 (Giddens et al., 2017), it has been shown that the integrity of astrocytic domains is compromised in models of epilepsy,

with changes that include overlapping of domains and/or the development of thicker processes or atrophy of the finer distal processes (Cho, Muthukumar, Stork, Coutinho-Budd, & Freeman, 2018; Khurgel & Ivy, 1996; Lenzer-Fanara, Li, Salerni, Payen, & Croll, 2017; Tashiro, Goldberg, & Yuste, 2002). In rats that experience status epilepticus, astrocytes have increased volume and activated morphology, although astrocyte numbers were not changed (Arisi et al., 2011). In neurodevelopmental diseases where astrocyte malfunction has been proposed as the causal factor, these diseases tend to go hand-in-hand with epileptic seizures (Hagerman & Stafstrom, 2009; Jian et al., 2006). Additionally, connexin expression was found to be changed during seizures in the hippocampus in a rat model of seizures (Laura, Xochitl, Anne, & Alberto, 2015), and astrocyte-specific Bestrophin-1 over-expression was found to restore generation of tonic GABA inhibition and suppress seizures in a mouse model of temporal lobe epilepsy (Pandit et al., 2020). Recently, a detailed study on the importance of astrocyte morphology and morphology-related genes in neurodegenerative disease revealed that reduction of astrocyte territory sizes was associated with changes in c-Fos expression in neurons and colocalization of pre- and postsynaptic markers (Endo et al., 2022). Overall, these studies provide evidence for astrocyte-specific disruptions in neuronal circuit regulation and/or abnormal neuronal organization associated with astrocyte dysfunction in the brain (Uhlmann et al., 2002). It would therefore be interesting to investigate how an epileptic phenotype affects astrocyte morphology in L1KO mice and whether rescue of the L1KO also rescues the deficits in astrocytic morphology and tiling seen in the mouse cortex. More recently, a study from the Deneen lab provides functional evidence for the importance of normal astrocyte morphology in learning and memory (Huang et al., 2021). Conditional deletion of nuclear factor I-A (NFIA), a transcription factor expressed in mature astrocytes, led to reduced astrocytic morphological complexity, impaired calcium signaling in the hippocampus, and deficits in learning and memory (Huang et al., 2021). Similar to NFIA, GPR37L1 is predominantly expressed in mature astrocytes and L1KO leads to reduced morphological complexity in cortical astrocytes. Because a limitation of this study is that it is highly descriptive, exploring the effect of L1KO in mice through behavioral studies such as the novel place or object recognition test or the Y maze test could potentially tie in the observed morphological and spatial deficits to behavioral outcomes.

Interestingly, the time period in which astrocytes start maturing coincides with the time period in which synapses are formed and refined. Indeed, astrocytes have been shown to play a crucial role in strengthening immature synapses and eliminating excess synapses that are not being used (Allen, 2013; Chung et al., 2015; Fossati, Matteoli, & Menna, 2020; Smith, Rutishauser, Silver, & Miller, 1990). There is now accumulating evidence that alterations to astrocyte morphogenesis and physiology can severely affect brain development and lead to neurological and neurodevelopmental disorders (Araujo et al., 2018; Giocanti-Auregan et al., 2016; Oberheim et al., 2009; Parikshak et al., 2013; Popov et al., 2021; Sloan & Barres, 2014). Some deficits that occur due to the dysfunction of astrocyte-neuron interactions during synaptogenesis and brain development include decreased neuronal process outgrowth and decreased synaptic function (Ballas, Lioy, Grunseich, & Mandel, 2009; Williams et al., 2014). Moreover, direct astrocytic contacts have been shown to regulate the local maturation of dendritic spines (Nishida & Okabe, 2007). Reciprocally,

the importance of proper astrocyte process maturation has been illustrated by the loss of neuronal dendritic maturation upon loss of astrocyte contact. When astrocytes are unable to contact neuronal synapses, there is reduced stability of dendritic protrusions (Nishida & Okabe, 2007).

The work presented here suggests that GPR37L1, an astrocyte-specific GPCR, plays an important role in the tiling and ramification of astrocytes during brain and astrocytic maturation in the mouse cortex. Loss of GPR37L1 leads to an increase in spacing between astrocytes in the adult mouse brain and the loss of complexity in astrocytic processes as seen via GFAP staining. Additionally, there is evidence for a developmental role of GPR37L1, as GPR37L1 is highly expressed in mature astrocytes in the human brain (Zhang et al., 2016) and knockout of GPR37L1 has been shown to lead to precocious development of Purkinje neurons of the cerebellum in the knockout mouse brain at P14-P17 (Marazziti et al., 2013). On top of this, human mutations in GPR37L1 lead to a seizure/epilepsy phenotype that manifests developmentally, and L1KO mice exhibit increased susceptibility to seizures (Giddens et al., 2017). It is therefore intriguing that our data suggest GPR37L1 plays an important role in brain development and, in particular, astrocyte maturation. Interestingly, however, loss of GPR37L1 does not affect excitatory synapse number, at least in the hippocampus (age P14-P16), indicating that deficits in astrocyte function due to the loss of GPR37L1 do not lead to reduced synaptic numbers (Jolly et al., 2018). Work from the same studies also revealed that there were no major differences in constitutive glutamate uptake in L1KO mouse brains. It is therefore possible that loss or dysfunction of GPR37L1 affects discrete aspects of the physiology of neurons and brain circuits instead of synapse numbers. This could be explored in future studies examining various aspects of neuronal function and development in the L1KO mice.

GPR37L1 is related to GPR37, a receptor that is most abundantly expressed in oligodendrocytes (Zhang et al., 2014; Yang et al., 2016). The degree of similarity between these two receptors suggests that they are likely to share a ligand. The secreted vertebrate protein prosaposin and its active fragment ("prosaptide") have been reported to bind to both GPR37L1 and GPR37 and activate their signaling (Meyer et al., 2013). Subsequently, activation of GPR37L1 and/or GPR37 by prosaptide was confirmed by several independent groups (Lundius et al., 2014; Jolly et al., 2017; Liu et al., 2018; Bang et al., 2018), although some investigators failed to detect significant activation of these receptors by prosaptide in transfected cells (Coleman et al., 2016). Studies by Kasparov and colleagues (Liu et al., 2018) suggested a resolution of these seemingly disparate findings by demonstrating that prosaptide stimulation of GPR37L1 is dependent on cellular context, being readily observed in astrocytes but more difficult to observe in heterologous cells over-expressing the receptor. Further work is needed to determine if prosaposin is indeed the primary ligand of GPR37L1 *in vivo* or instead represents more of a modulator of GPR37L1 function. Relevant to the current studies, little is known about the effects of prosaposin on astrocytic development, but the data presented here suggest that future experiments in this area may be of interest.

It is important to note that the immunopanned astrocytes in our studies were cultured in serum-free astrocyte media, as the addition of serum (such as FBS) induces a reactive phenotype in astrocytes (Cahoy et al., 2008; Codeluppi et al., 2011; Doyle et al., 2008; Foo

et al., 2011; Prah et al., 2019). Thus, there may be lower levels of the putative GPR37L1 ligand prosaposin in the culture media for these immunopanned astrocytes relative to FBS-treated astrocytes. However, prosaposin is known to be secreted by cells in culture, and therefore GPR37L1 is likely to exhibit at least some degree of constitutive activity even in serum-free culture conditions, with the level of constitutive activity likely being influenced by factors such as cell density (Coleman et al., 2016; Liu et al., 2018). It is therefore important to note that the observed phenotypic effects of L1KO *in vitro* may be dependent on the cell culture conditions utilized.

In summary, while some information is known about the molecular mechanisms that control the early differentiation of immature astrocytes (Deneen et al., 2006; P. Kang et al., 2012; Kohyama et al., 2010), little is known about the molecular mechanisms regulating the later stages of astrocyte maturation. Moreover, the mechanisms controlling the establishment of astrocyte morphology are not well-understood. The data presented here provide evidence for an important role of GPR37L1 in the regulation of astrocytic morphology and tiling during development. In particular, our findings suggest that expression of GPR37L1 is more important for later astrocytic maturation than for early astrocytic maturation. Further work in this area could help to elucidate the specific downstream pathways activated by GPR37L1 that are involved in the regulation of astrocyte maturation during development. Moreover, given the genetic links between GPR37L1 and epilepsy (Giddens et al., 2017; Dershem et al., 2019), these findings are relevant to epilepsy, which affects over 65 million people worldwide (Hesdorffer et al., 2011). Current medications used to treat epilepsy often have adverse side effects and/or are not effective, and thus it is necessary to identify new drug targets that may allow for the design of novel therapies with fewer off-target effects. Epilepsy has traditionally been viewed as a neurological disease that specifically affects neurons, but there has been growing evidence for an astrocytic basis of epilepsy (Barbaro, Takahashi, & Baraban, 2004; DiNuzzo, Mangia, Maraviglia, & Giove, 2014; N. Kang, Xu, Xu, Nedergaard, & Kang, 2005; Rogawski, 2005; Tian et al., 2005). The evidence presented here for a key role of GPR37L1 in brain development and astrocytic maturation suggests that GPR37L1 may be a target of interest for future therapies aimed at treating epilepsy and other seizure disorders.

Supplementary Material

Refer to Web version on PubMed Central for supplementary material.

ACKNOWLEDGMENTS

REFERENCES

Afgan E, Baker D, Batut B, van den Beek M, Bouvier D, Cech M, … Blankenberg D. (2018). The Galaxy platform for accessible, reproducible and collaborative biomedical analyses: 2018 update. Nucleic Acids Res, 46(W1), W537–W544. doi:10.1093/nar/gky379 [PubMed: 29790989]

Allen NJ (2013). Role of glia in developmental synapse formation. Curr Opin Neurobiol, 23(6), 1027–1033. doi:10.1016/j.conb.2013.06.004 [PubMed: 23871217]

Anderson MA, Burda JE, Ren Y, Ao Y, O'Shea TM, Kawaguchi R, … Sofroniew MV (2016). Astrocyte scar formation aids central nervous system axon regeneration. Nature, 532(7598), 195–200. doi:10.1038/nature17623 [PubMed: 27027288]

Araujo BHS, Kaid C, De Souza JS, Gomes da Silva S, Goulart E, Caires LCJ, … Cavalheiro EA (2018). Down Syndrome iPSC-Derived Astrocytes Impair Neuronal Synaptogenesis and the mTOR Pathway In Vitro. Mol Neurobiol, 55(7), 5962–5975. doi:10.1007/s12035-017-0818-6 [PubMed: 29128905]

Arisi GM, Ruch M, Foresti ML, Mukherjee S, Ribak CE, & Shapiro LA (2011). Astrocyte Alterations in the Hippocampus Following Pilocarpine-induced Seizures in Aged Rats. Aging Dis, 2(4), 294–300. Retrieved from https://www.ncbi.nlm.nih.gov/pubmed/22396881 [PubMed: 22396881]

Ballas N, Lioy DT, Grunseich C, & Mandel G. (2009). Non-cell autonomous influence of MeCP2-deficient glia on neuronal dendritic morphology. Nat Neurosci, 12(3), 311–317. doi:10.1038/nn.2275 [PubMed: 19234456]

Bang S, Xie YK, Zhang ZJ, Wang Z, Xu ZZ, Ji RR (2018). GPR37 regulates macrophage phagocytosis and resolution of inflammatory pain. J Clin Invest, 128(8), 3568–3582. doi:10.1172/JCI99888 [PubMed: 30010619]

Barbaro NM, Takahashi DK, & Baraban SC (2004). A potential role for astrocytes in mediating the antiepileptic actions of furosemide in vitro. Neuroscience, 128(3), 655–663. doi:10.1016/j.neuroscience.2004.07.007 [PubMed: 15381293]

Behar TN (2001). Analysis of fractal dimension of O2A glial cells differentiating in vitro. Methods, 24(4), 331–339. doi:10.1006/meth.2001.1203 [PubMed: 11465998]

Bernardinelli Y, Randall J, Janett E, Nikonenko I, Konig S, Jones EV, … Muller D. (2014). Activity-dependent structural plasticity of perisynaptic astrocytic domains promotes excitatory synapse stability. Curr Biol, 24(15), 1679–1688. doi:10.1016/j.cub.2014.06.025 [PubMed: 25042585]

Binley KE, Ng WS, Tribble JR, Song B, & Morgan JE (2014). Sholl analysis: a quantitative comparison of semi-automated methods. J Neurosci Methods, 225, 65–70. doi:10.1016/j.jneumeth.2014.01.017 [PubMed: 24485871]

Buffo A, Rite I, Tripathi P, Lepier A, Colak D, Horn AP, … Gotz M. (2008). Origin and progeny of reactive gliosis: A source of multipotent cells in the injured brain. Proc Natl Acad Sci U S A, 105(9), 3581–3586. doi:10.1073/pnas.0709002105 [PubMed: 18299565]

Bushong EA, Martone ME, & Ellisman MH (2004). Maturation of astrocyte morphology and the establishment of astrocyte domains during postnatal hippocampal development. Int J Dev Neurosci, 22(2), 73–86. doi:10.1016/j.ijdevneu.2003.12.008 [PubMed: 15036382]

Bushong EA, Martone ME, Jones YZ, & Ellisman MH (2002). Protoplasmic astrocytes in CA1 stratum radiatum occupy separate anatomical domains. J Neurosci, 22(1), 183–192. Retrieved from https://www.ncbi.nlm.nih.gov/pubmed/11756501 [PubMed: 11756501]

Cahoy JD, Emery B, Kaushal A, Foo LC, Zamanian JL, Christopherson KS, … Barres BA (2008). A transcriptome database for astrocytes, neurons, and oligodendrocytes: a new resource for understanding brain development and function. J Neurosci, 28(1), 264–278. doi:10.1523/JNEUROSCI.4178-07.2008 [PubMed: 18171944]

Carlen M, Meletis K, Goritz C, Darsalia V, Evergren E, Tanigaki K, … Frisen J. (2009). Forebrain ependymal cells are Notch-dependent and generate neuroblasts and astrocytes after stroke. Nat Neurosci, 12(3), 259–267. doi:10.1038/nn.2268 [PubMed: 19234458]

Chang Ling T, & Stone J. (1991). Factors determining the morphology and distribution of astrocytes in the cat retina: a 'contact-spacing' model of astrocyte interaction. J Comp Neurol, 303(3), 387–399. doi:10.1002/cne.903030305 [PubMed: 2007656]

Cho S, Muthukumar AK, Stork T, Coutinho-Budd JC, & Freeman MR (2018). Focal adhesion molecules regulate astrocyte morphology and glutamate transporters to suppress seizure-like behavior. Proc Natl Acad Sci U S A, 115(44), 11316–11321. doi:10.1073/pnas.1800830115 [PubMed: 30327343]

Chung WS, Allen NJ, & Eroglu C. (2015). Astrocytes Control Synapse Formation, Function, and Elimination. Cold Spring Harb Perspect Biol, 7(9), a020370. doi:10.1101/cshperspect.a020370

Chung WS, Clarke LE, Wang GX, Stafford BK, Sher A, Chakraborty C, … Barres BA (2013). Astrocytes mediate synapse elimination through MEGF10 and MERTK pathways. Nature, 504, 394–400. [PubMed: 24270812]

Clarke LE, Liddelow SA, Chakraborty C, Munch AE, Heiman M, & Barres BA (2018). Normal aging induces A1-like astrocyte reactivity. Proc Natl Acad Sci U S A, 115(8), E1896–E1905. doi:10.1073/pnas.1800165115 [PubMed: 29437957]

Codeluppi S, Gregory EN, Kjell J, Wigerblad G, Olson L, & Svensson CI (2011). Influence of rat substrain and growth conditions on the characteristics of primary cultures of adult rat spinal cord astrocytes. J Neurosci Methods, 197(1), 118–127. doi:10.1016/j.jneumeth.2011.02.011 [PubMed: 21345349]

Coleman JLJ, Ngo T, Schmidt J, Mrad N, Liew CK, Jones NM, Graham RM, Smith NJ (2016). Metalloprotease cleavage of the N terminus of the orphan G protein-coupled receptor GPR37L1 reduces its constitutive activity. Sci Signal, 9(423):ra36. doi:10.1126/scisignal.aad1089

Connor JR, & Berkowitz EM (1985). A demonstration of glial filament distribution in astrocytes isolated from rat cerebral cortex. Neuroscience, 16(1), 33–44. [PubMed: 2423916]

Deneen B, Ho R, Lukaszewicz A, Hochstim CJ, Gronostajski RM, & Anderson DJ (2006). The transcription factor NFIA controls the onset of gliogenesis in the developing spinal cord. Neuron, 52(6), 953–968. doi:10.1016/j.neuron.2006.11.019 [PubMed: 17178400]

Dershem R, Metpally RPR, Jeffreys K, Krishnamurthy S, Smelser DT, Hershfinkel M, … Breitwieser GE (2019). Rare-variant pathogenicity triage and inclusion of synonymous variants improves analysis of disease associations of orphan G protein-coupled receptors. J Biol Chem, 294(48), 18109–18121. doi:10.1074/jbc.RA119.009253 [PubMed: 31628190]

DiNuzzo M, Mangia S, Maraviglia B, & Giove F. (2014). Physiological bases of the K+ and the glutamate/GABA hypotheses of epilepsy. Epilepsy Res, 108(6), 995–1012. doi:10.1016/j.eplepsyres.2014.04.001 [PubMed: 24818957]

Dobin A, Davis CA, Schlesinger F, Drenkow J, Zaleski C, Jha S, … Gingeras TR (2013). STAR: ultrafast universal RNA-seq aligner. Bioinformatics, 29(1), 15–21. doi:10.1093/bioinformatics/bts635 [PubMed: 23104886]

Doyle JP, Dougherty JD, Heiman M, Schmidt EF, Stevens TR, Ma G, … Heintz N. (2008). Application of a translational profiling approach for the comparative analysis of CNS cell types. Cell, 135(4), 749–762. doi:10.1016/j.cell.2008.10.029 [PubMed: 19013282]

Dreher Z, Tout S, & Stone J. (1994). Interactions of living astrocytes in vitro: evidence of the development of contact spacing. Glia, 11(1), 57–63. doi:10.1002/glia.440110108 [PubMed: 8070895]

Endo F, Kasai A, Soto JS, Yu X, Qu Z, Hashimoto H, … Khakh BS (2022). Molecular basis of astrocyte diversity and morphology across the CNS in health and disease. Science, 378(6619), eadc9020. doi:10.1126/science.adc9020.

Escartin C, Galea E, Lakatos A, O'Callaghan JP, Petzold GC, Serrano-Pozo A, Steinhäuser C, Volterra A, Carmignoto G, Agarwal A, Allen NJ, Araque A, Barbeito L, Barzilai A, Bergles DE, Bonvento G, Butt AM, Chen WT, Cohen-Salmon M, Cunningham C, … Verkhratsky A. (2021). Reactive astrocyte nomenclature, definitions, and future directions. Nature Neuroscience, 24(3), 312–325. doi:10.1038/s41593-020-00783-4 [PubMed: 33589835]

Flugge G, Araya-Callis CG-R,E, Stadelmann-Nessler C, & Fuchs E. (2014). NDRG2 as a marker protein for brain astrocytes. Cell and Tissue Research 357, 31–41. [PubMed: 24816982]

Foo LC (2013). Purification of rat and mouse astrocytes by immunopanning. Cold Spring Harb Protoc, 2013(5), 421–432. doi:10.1101/pdb.prot074211 [PubMed: 23637363]

Foo LC, Allen NJ, Bushong EA, Ventura PB, Chung WS, Zhou L, … Barres BA (2011). Development of a novel method for the purification and culture of rodent astrocytes. Neuron, 71(5), 799–811. [PubMed: 21903074]

Fossati G, Matteoli M, & Menna E. (2020). Astrocytic Factors Controlling Synaptogenesis: A Team Play. Cells, 9(10). doi:10.3390/cells9102173

Freeman MR (2010). Specification and morphogenesis of astrocytes. Science, 330(6005), 774–778. doi:10.1126/science.1190928 [PubMed: 21051628]

Giddens MM, Wong JC, Schroeder JP, Farrow EG, Smith BM, Owino S, … Hall RA (2017). GPR37L1 modulates seizure susceptibility: Evidence from mouse studies and analyses of a human GPR37L1 variant. Neurobiol Dis, 106, 181–190. doi:10.1016/j.nbd.2017.07.006 [PubMed: 28688853]

Giocanti-Auregan A, Vacca O, Benard R, Cao S, Siqueiros L, Montanez C, … Tadayoni R. (2016). Altered astrocyte morphology and vascular development in dystrophin-Dp71-null mice. Glia, 64(5), 716–729. doi:10.1002/glia.22956 [PubMed: 26711882]

Hagerman PJ, & Stafstrom CE (2009). Origins of epilepsy in fragile X syndrome. Epilepsy Curr, 9(4), 108–112. doi:10.1111/j.1535-7511.2009.01309.x [PubMed: 19693328]

Heindl S, Gesierich B, Benakis C, Llovera G, Duering M, & Liesz A. (2018). Automated Morphological Analysis of Microglia After Stroke. Front Cell Neurosci, 12, 106. doi:10.3389/fncel.2018.00106 [PubMed: 29725290]

Hesdorffer DC, Logroscino G, Benn EK, Katri N, Cascino G, & Hauser WA (2011). Estimating risk for developing epilepsy: a population-based study in Rochester, Minnesota. Neurology, 76(1), 23–27. doi:10.1212/WNL.0b013e318204a36a [PubMed: 21205691]

Hirrlinger J, Hulsmann S, & Kirchhoff F. (2004). Astroglial processes show spontaneous motility at active synaptic terminals in situ. Eur J Neurosci, 20(8), 2235–2239. doi:10.1111/j.1460-9568.2004.03689.x [PubMed: 15450103]

Hong YM, Jo DG, Lee MC, Kim SY, & Jung YK (2003). Reduced expression of calsenilin/DREAM/KChIP3 in the brains of kainic acid-induced seizure and epilepsy patients. Neurosci Lett, 340(1), 33–36. doi:10.1016/s0304-3940(03)00067-3 [PubMed: 12648752]

Huang AY, Woo J, Sardar D, Lozzi B, Bosquez Huerta NA, Lin CJ, Felice D, Jain A, Paulucci-Holthauzen A, & Deneen B. (2020). Region-Specific Transcriptional Control of Astrocyte Function Oversees Local Circuit Activities. Neuron, 106(6), 992–1008.e9. doi:10.1016/j.neuron.2020.03.025 [PubMed: 32320644]

Jian L, Nagarajan L, de Klerk N, Ravine D, Bower C, Anderson A, … Leonard H. (2006). Predictors of seizure onset in Rett syndrome. J Pediatr, 149(4), 542–547. doi:10.1016/j.jpeds.2006.06.015 [PubMed: 17011329]

Jiang C, Li L, Wu M, Hao M, & Feng J. (2021). Association of KCNJ10 variants and the susceptibility to clinical epilepsy. Clin Neurol Neurosurg, 200, 106340. doi:10.1016/j.clineuro.2020.106340 [PubMed: 33187755]

Jolly S, Bazargani N, Quiroga AC, Pringle NP, Attwell D, Richardson WD, & Li H. (2018). G protein-coupled receptor 37-like 1 modulates astrocyte glutamate transporters and neuronal NMDA receptors and is neuroprotective in ischemia. Glia, 66(1), 47–61. doi:10.1002/glia.23198 [PubMed: 28795439]

Kalman M. (2002). GFAP expression withdraws--a trend of glial evolution? Brain Res Bull, 57(3–4), 509–511. doi:10.1016/s0361-9230(01)00713-4 [PubMed: 11923020]

Kang N, Xu J, Xu Q, Nedergaard M, & Kang J. (2005). Astrocytic glutamate release-induced transient depolarization and epileptiform discharges in hippocampal CA1 pyramidal neurons. J Neurophysiol, 94(6), 4121–4130. doi:10.1152/jn.00448.2005 [PubMed: 16162834]

Kang P, Lee HK, Glasgow SM, Finley M, Donti T, Gaber ZB, … Deneen B. (2012). Sox9 and NFIA coordinate a transcriptional regulatory cascade during the initiation of gliogenesis. Neuron, 74(1), 79–94. doi:10.1016/j.neuron.2012.01.024 [PubMed: 22500632]

Khurgel M, & Ivy GO (1996). Astrocytes in kindling: relevance to epileptogenesis. Epilepsy Res, 26(1), 163–175. doi:10.1016/s0920-1211(96)00051-4 [PubMed: 8985698]

Kohyama J, Sanosaka T, Tokunaga A, Takatsuka E, Tsujimura K, Okano H, & Nakashima K. (2010). BMP-induced REST regulates the establishment and maintenance of astrocytic identity. J Cell Biol, 189(1), 159–170. doi:10.1083/jcb.200908048 [PubMed: 20351065]

Kongsui R, Beynon SB, Johnson SJ, & Walker FR (2014). Quantitative assessment of microglial morphology and density reveals remarkable consistency in the distribution and morphology of cells within the healthy prefrontal cortex of the rat. Journal of Neuroinflammation, 11, 182. [PubMed: 25343964]

Author Manuscript Author Manuscript Author Manuscript Author Manuscript

Laura MC, Xochitl FP, Anne S, & Alberto MV (2015). Analysis of connexin expression during seizures induced by 4-aminopyridine in the rat hippocampus. J Biomed Sci, 22, 69. doi:10.1186/s12929-015-0176-5 [PubMed: 26268619]

Lee E, & Chung WS (2019). Glial Control of Synapse Number in Healthy and Diseased Brain. Front Cell Neurosci, 13, 42. doi:10.3389/fncel.2019.00042 [PubMed: 30814931]

Legland D, Arganda-Carreras I, & Andrey P. (2016). MorphoLibJ: integrated library and plugins for mathematical morphology with ImageJ. Bioinformatics, 32(22), 3532–3534. doi:10.1093/bioinformatics/btw413 [PubMed: 27412086]

Lenzer-Fanara JR, Li T, Salerni EA, Payen F, & Croll SD (2017). VEGF treatment during status epilepticus attenuates long-term seizure-associated alterations in astrocyte morphology. Epilepsy Behav, 70(Pt A), 33–44. doi:10.1016/j.yebeh.2017.02.019 [PubMed: 28410463]

Li J, Khankan RR, Caneda C, Godoy MI, Haney MS, Krawczyk MC, … Zhang Y. (2019). Astrocyte-to-astrocyte contact and a positive feedback loop of growth factor signaling regulate astrocyte maturation. Glia, 67(8), 1571–1597. doi:10.1002/glia.23630 [PubMed: 31033049]

Liao Y, Smyth GK, & Shi W. (2014). featureCounts: an efficient general purpose program for assigning sequence reads to genomic features. Bioinformatics, 30(7), 923–930. doi:10.1093/bioinformatics/btt656 [PubMed: 24227677]

Liddelow SA, & Barres BA (2017). Reactive Astrocytes: Production, Function, and Therapeutic Potential. Immunity, 46(6), 957–967. doi:10.1016/j.immuni.2017.06.006 [PubMed: 28636962]

Liddelow SA, Guttenplan KA, Clarke LE, Bennett FC, Bohlen CJ, Schirmer L, … Barres BA (2017). Neurotoxic reactive astrocytes are induced by activated microglia. Nature, 541(7638), 481–487. doi:10.1038/nature21029 [PubMed: 28099414]

Liu B, Mosienko V, Cardoso BV, Prokudina D, Huentelman M, Teschemacher AG, Kasparov S. (2018). Glio- and neuro-protection by prosaposin is mediated by orphan G-protein coupled receptors GPR37L1 and GPR37. Glia, 66(11), 2414–2426. doi:10.1002/glia.23480 [PubMed: 30260505]

Love MI, Huber W, & Anders S. (2014). Moderated estimation of fold change and dispersion for RNA-seq data with DESeq2. Genome Biol, 15(12), 550. doi:10.1186/s13059-014-0550-8 [PubMed: 25516281]

Lundius EG, Vukojevic V, Hertz E, Stroth N, Cederlund A, Hiraiwa M, Terenius L, Svenningsson P. (2014) GPR37 protein trafficking to the plasma membrane regulated by prosaposin and GM1 gangliosides promotes cell viability. J Biol Chem, 289(8), 4660–4673. doi:10.1074/jbc.M113.510883 [PubMed: 24371137]

Mahata SK, Gruber B, Mahata M, Roder C, Fischer-Colbrie R, & Sperk G. (1993). Kainic acid seizures in the rat: differential expression of chromogranin A, carboxypeptidase H and peptidylglycine alpha-amidating monooxigenase in subfields of the hippocampal formation. Acta Neuropathol, 86(6), 590–595. doi:10.1007/BF00294297 [PubMed: 8310814]

Malatesta P, Appolloni I, & Calzolari F. (2008). Radial glia and neural stem cells. Cell Tissue Res, 331(1), 165–178. doi:10.1007/s00441-007-0481-8 [PubMed: 17846796]

Marazziti D, Di Pietro C, Golini E, Mandillo S, La Sala G, Matteoni R, & Tocchini-Valentini GP (2013). Precocious cerebellum development and improved motor functions in mice lacking the astrocyte cilium-, patched 1-associated Gpr37l1 receptor. Proc Natl Acad Sci U S A, 110(41), 16486–16491. doi:10.1073/pnas.1314819110 [PubMed: 24062445]

McCarthy KD, & de Vellis J. (1980). Preparation of separate astroglial and oligodendroglial cell cultures from rat cerebral tissue. J Cell Biol, 85(3), 890–902. doi:10.1083/jcb.85.3.890 [PubMed: 6248568]

Meyer RC, Giddens MM, Schaefer SA, Hall RA (2013). GPR37 and GPR37L1 are receptors for the neuroprotective and glioprotective factors prosaptide and prosaposin. Proc Natl Acad Sci U S A, 110(23), 9529–9534. doi:10.1073/pnas.1219004110 [PubMed: 23690594]

Meyerink BL, Tiwari NK, & Pilaz LJ (2020). Ariadne's Thread in the Developing Cerebral Cortex: Mechanisms Enabling the Guiding Role of the Radial Glia Basal Process during Neuron Migration. Cells, 10(1). doi:10.3390/cells10010003

Author Manuscript Author Manuscript Author Manuscript Author Manuscript

Mir A, Chaudhary M, Alkhaldi H, Alhazmi R, Albaradie R, & Housawi Y. (2019). Epilepsy in patients with EAST syndrome caused by mutation in the KCNJ10. Brain Dev, 41(8), 706–715. doi:10.1016/j.braindev.2019.03.009 [PubMed: 30952461]

Molofsky AV, Krencik R, Ullian EM, Tsai HH, Deneen B, Richardson WD, … Rowitch DH (2012). Astrocytes and disease: a neurodevelopmental perspective. Genes Dev, 26(9), 891–907. doi:10.1101/gad.188326.112 [PubMed: 22549954]

Morrison RS, & de Vellis J. (1981). Growth of purified astrocytes in a chemically defined medium. Proc Natl Acad Sci U S A, 78(11), 7205–7209. doi:10.1073/pnas.78.11.7205 [PubMed: 6458820]

Moya-Mendez ME, Mueller DM, Pratt M, Bonner M, Elliott C, Hunanyan A, … Mikati MA (2021). Early onset severe ATP1A2 epileptic encephalopathy: Clinical characteristics and underlying mutations. Epilepsy Behav, 116, 107732. doi:10.1016/j.yebeh.2020.107732

Moye SL, Diaz-Castro B, Gangwani MR, & Khakh BS (2019). Visualizing astrocyte morphology using lucifer yellow iontophoresis. Journal of Visualized Experiments, 151, e60225.

Naskar S, & Chattarji S. (2019). Stress Elicits Contrasting Effects on the Structure and Number of Astrocytes in the Amygdala versus Hippocampus. eNeuro, 6(1). doi:10.1523/ENEURO.0338-18.2019

Nguyen TT, Dammer EB, Owino SA, Giddens MM, Madaras NS, Duong DM, … Hall RA (2020). Quantitative Proteomics Reveal an Altered Pattern of Protein Expression in Brain Tissue from Mice Lacking GPR37 and GPR37L1. J Proteome Res, 19(2), 744–755. doi:10.1021/acs.jproteome.9b00622 [PubMed: 31903766]

Nishida H, & Okabe S. (2007). Direct astrocytic contacts regulate local maturation of dendritic spines. J Neurosci, 27(2), 331–340. doi:10.1523/JNEUROSCI.4466-06.2007 [PubMed: 17215394]

Nishiyama A, Komitova M, Suzuki R, & Zhu X. (2009). Polydendrocytes (NG2 cells): multifunctional cells with lineage plasticity. Nat Rev Neurosci, 10(1), 9–22. doi:10.1038/nrn2495 [PubMed: 19096367]

Nishiyama A, Suzuki R, & Zhu X. (2014). NG2 cells (polydendrocytes) in brain physiology and repair. Front Neurosci, 8, 133. doi:10.3389/fnins.2014.00133 [PubMed: 25018689]

Nishiyama A, Watanabe M, Yang Z, & Bu J. (2002). Identity, distribution, and development of polydendrocytes: NG2-expressing glial cells. J Neurocytol, 31(6–7), 437–455. doi:10.1023/a:12651 [PubMed: 14501215]

Oberheim NA, Takano T, Han X, He W, Lin JH, Wang F, … Nedergaard M. (2009). Uniquely hominid features of adult human astrocytes. J Neurosci, 29(10), 3276–3287. doi:10.1523/JNEUROSCI.4707-08.2009 [PubMed: 19279265]

Pandit S, Neupane C, Woo J, Sharma R, Nam MH, Lee GS, Yi MH, Shin N, Kim DW, Cho H, Jeon BH, Kim HW, Lee CJ, & Park JB (2020). Bestrophin1-mediated tonic GABA release from reactive astrocytes prevents the development of seizure-prone network in kainate-injected hippocampi. Glia, 68(5), 1065–1080. doi:10.1002/glia.23762 [PubMed: 31833596]

Parikshak NN, Luo R, Zhang A, Won H, Lowe JK, Chandran V, … Geschwind DH (2013). Integrative functional genomic analyses implicate specific molecular pathways and circuits in autism. Cell, 155(5), 1008–1021. doi:10.1016/j.cell.2013.10.031 [PubMed: 24267887]

Popov A, Brazhe A, Denisov P, Sutyagina O, Li L, Lazareva N, … Semyanov A. (2021). Astrocyte dystrophy in ageing brain parallels impaired synaptic plasticity. Aging Cell, 20(3), e13334. doi:10.1111/acel.13334

Prah J, Winters A, Chaudhari K, Hersh J, Liu R, & Yang SH (2019). A novel serum free primary astrocyte culture method that mimic quiescent astrocyte phenotype. J Neurosci Methods, 320, 50–63. doi:10.1016/j.jneumeth.2019.03.013 [PubMed: 30904500]

Quinlan RA, Brenner M, Goldman JE, & Messing A. (2007). GFAP and its role in Alexander disease. Exp Cell Res, 313(10), 2077–2087. doi:10.1016/j.yexcr.2007.04.004 [PubMed: 17498694]

Reichold M, Zdebik AA, Lieberer E, Rapedius M, Schmidt K, Bandulik S, … Warth R. (2010). KCNJ10 gene mutations causing EAST syndrome (epilepsy, ataxia, sensorineural deafness, and tubulopathy) disrupt channel function. Proc Natl Acad Sci U S A, 107(32), 14490–14495. doi:10.1073/pnas.1003072107 [PubMed: 20651251]

Rogawski MA (2005). Astrocytes get in the act in epilepsy. Nat Med, 11(9), 919–920. doi:10.1038/nm0905-919 [PubMed: 16145568]

Schindelin J, Arganda-Carreras I, Frise E, Kaynig V, Longair M, Pietzsch T, … Cardona A. (2012). Fiji: an open-source platform for biological-image analysis. Nat Methods, 9(7), 676–682. doi:10.1038/nmeth.2019 [PubMed: 22743772]

Sethi P, Virmani G, Gupta K, Thumu SCR, Ramanan N, & Marathe S. (2021). Automated morphometric analysis with SMorph software reveals plasticity induced by antidepressant therapy in hippocampal astrocytes. J Cell Sci, 134(12). doi:10.1242/jcs.258430

SheikhBahaei S, Morris B, Collina J, Anjum S, Znati S, Gamarra J, … Smith JC (2018). Morphometric analysis of astrocytes in brainstem respiratory regions. J Comp Neurol, 526(13), 2032–2047. doi:10.1002/cne.24472 [PubMed: 29888789]

Sherman BT, Hao M, Qiu J, Jiao X, Baseler MW, Lane HC, … Chang W. (2022). DAVID: a web server for functional enrichment analysis and functional annotation of gene lists (2021 update). Nucleic Acids Res. doi:10.1093/nar/gkac194

Shin HJ, Jeong EA, Lee JY, An HS, Jang HM, Ahn YJ, … Roh GS (2021). Lipocalin-2 Deficiency Reduces Oxidative Stress and Neuroinflammation and Results in Attenuation of Kainic Acid-Induced Hippocampal Cell Death. Antioxidants (Basel), 10(1). doi:10.3390/antiox10010100

Sholl DA (1953). Dendritic organization in the neurons of the visual and motor cortices of the cat. J Anat, 87(4), 387–406. Retrieved from https://www.ncbi.nlm.nih.gov/pubmed/13117757 [PubMed: 13117757]

Sloan SA, & Barres BA (2014). Mechanisms of astrocyte development and their contributions to neurodevelopmental disorders. Curr Opin Neurobiol, 27, 75–81. doi:10.1016/j.conb.2014.03.005 [PubMed: 24694749]

Sloan SA, Darmanis S, Huber N, Khan TA, Birey F, Caneda C, … Pasca SP (2017). Human Astrocyte Maturation Captured in 3D Cerebral Cortical Spheroids Derived from Pluripotent Stem Cells. Neuron, 95(4), 779–790 e776. doi:10.1016/j.neuron.2017.07.035 [PubMed: 28817799]

Smith GM, Rutishauser U, Silver J, & Miller RH (1990). Maturation of astrocytes in vitro alters the extent and molecular basis of neurite outgrowth. Dev Biol, 138(2), 377–390. doi:10.1016/0012-1606(90)90204-v [PubMed: 2318341]

Tashiro A, Goldberg J, & Yuste R. (2002). Calcium oscillations in neocortical astrocytes under epileptiform conditions. J Neurobiol, 50(1), 45–55. doi:10.1002/neu.10019 [PubMed: 11748632]

Tian GF, Azmi H, Takano T, Xu Q, Peng W, Lin J, … Nedergaard M. (2005). An astrocytic basis of epilepsy. Nat Med, 11(9), 973–981. doi:10.1038/nm1277 [PubMed: 16116433]

Tiane A, Schepers M, Rombaut B, Hupperts R, Prickaerts J, Hellings N, … Vanmierlo T. (2019). From OPC to Oligodendrocyte: An Epigenetic Journey. Cells, 8(10). doi:10.3390/cells8101236

Tout S, Dreher Z, Chan-Ling T, & Stone J. (1993). Contact-spacing among astrocytes is independent of neighbouring structures: in vivo and in vitro evidence. J Comp Neurol, 332(4), 433–443. doi:10.1002/cne.903320405 [PubMed: 8349842]

Turrero Garcia M, & Harwell CC (2017). Radial glia in the ventral telencephalon. FEBS Lett, 591(24), 3942–3959. doi:10.1002/1873-3468.12829 [PubMed: 28862741]

Uhlmann EJ, Wong M, Baldwin RL, Bajenaru ML, Onda H, Kwiatkowski DJ, … Gutmann DH (2002). Astrocyte-specific TSC1 conditional knockout mice exhibit abnormal neuronal organization and seizures. Ann Neurol, 52(3), 285–296. doi:10.1002/ana.10283 [PubMed: 12205640]

Varvel NH, Grathwohl SA, Baumann F, Liebig C, Bosch A, Brawek B, … Jucker M. (2012). Microglial repopulation model reveals a robust homeostatic process for replacing CNS myeloid cells. Proc Natl Acad Sci U S A, 109(44), 18150–18155. doi:10.1073/pnas.1210150109 [PubMed: 23071306]

Vasile F, Dossi E, & Rouach N. (2017). Human astrocytes: structure and functions in the healthy brain. Brain Struct Funct, 222(5), 2017–2029. doi:10.1007/s00429-017-1383-5 [PubMed: 28280934]

Vetro A, Nielsen HN, Holm R, Hevner RF, Parrini E, Powis Z, … collaborators, A. A. A. (2021). ATP1A2- and ATP1A3-associated early profound epileptic encephalopathy and polymicrogyria. Brain, 144(5), 1435–1450. doi:10.1093/brain/awab052 [PubMed: 33880529]

Visanji NP, Wong JC, Wang SX, Cappel B, Kleinschmidt-Demasters BK, Handler MH, … Hazrati LN (2012). A proteomic analysis of pediatric seizure cases associated with astrocytic inclusions. Epilepsia, 53(3), e50–54. doi:10.1111/j.1528-1167.2011.03369.x [PubMed: 22220588]

Williams EC, Zhong X, Mohamed A, Li R, Liu Y, Dong Q, … Chang Q. (2014). Mutant astrocytes differentiated from Rett syndrome patients-specific iPSCs have adverse effects on wild-type neurons. Hum Mol Genet, 23(11), 2968–2980. doi:10.1093/hmg/ddu008 [PubMed: 24419315]

Xu C, Funahashi Y, Watanabe T, Takano T, Nakamuta S, Namba T, & Kaibuchi K. (2015). Radial glial cell-neuron interaction directs axon formation at the opposite side of the neuron from the contact site. J Neurosci, 43, 14517–14532.

Yang HJ, Vainshtein A, Maik-Rachline G, Peles E. (2016). G protein-coupled receptor 37 is a negative regulator of oligodendrocyte differentiation and myelination. Nat Comm, 7, 10884. doi:10.1038/ncomms10884

Yin A, Guo H, Tao L, Cai G, Wang Y, Yao L, … Li Y. (2020). NDRG2 Protects the Brain from Excitotoxicity by Facilitating Interstitial Glutamate Uptake. Transl Stroke Res, 11(2), 214–227. doi:10.1007/s12975-019-00708-9 [PubMed: 31250377]

Zamanian JL, Xu L, Foo LC, Nouri N, Zhou L, Giffard RG, & Barres BA (2012). Genomic analysis of reactive astrogliosis. J Neurosci, 32(18), 6391–6410. doi:10.1523/JNEUROSCI.6221-11.2012 [PubMed: 22553043]

Zarei-Kheirabadi M, Vaccaro AR, Rahimi-Movaghar V, Kiani S, & Baharvand H. (2020). An Overview of Extrinsic and Intrinsic Mechanisms Involved in Astrocyte Development in the Central Nervous System. Stem Cells Dev, 29(5), 266–280. doi:10.1089/scd.2019.0189 [PubMed: 31847709]

Zhang Y, Chen K, Sloan SA, Bennett ML, Scholze AR, O'Keeffe S, … Wu JQ (2014). An RNA-sequencing transcriptome and splicing database of glia, neurons, and vascular cells of the cerebral cortex. J Neurosci, 34(36), 11929–11947. doi:10.1523/JNEUROSCI.1860-14.2014 [PubMed: 25186741]

Zhang Y, Sloan SA, Clarke LE, Caneda C, Plaza CA, Blumenthal PD, … Barres BA (2016). Purification and Characterization of Progenitor and Mature Human Astrocytes Reveals Transcriptional and Functional Differences with Mouse. Neuron, 89(1), 37–53. doi:10.1016/j.neuron.2015.11.013 [PubMed: 26687838]

Zhou B, Zuo YX, & Jiang RT (2019). Astrocyte morphology: Diversity, plasticity, and role in neurological diseases. CNS Neurosci Ther, 25(6), 665–673. doi:10.1111/cns.13123 [PubMed: 30929313]

Zhou J, Tao K, Guo K, Wu L, Zhang Z, Feng D, … Qin H. (2020). Suppression of NDRG2 alleviates brain injury after intracerebral hemorrhage through mitigating astrocyte-drived glutamate neurotoxicity via NF-kappaB/GLT1 signaling. Brain Res, 1729, 146600. doi:10.1016/j.brainres.2019.146600

Zhou J, Wu YC, Xiao BJ, Guo XD, Zheng QX, & Wu B. (2019). Age-related Changes in the Global DNA Methylation Profile of Oligodendrocyte Progenitor Cells Derived from Rat Spinal Cords. Curr Med Sci, 39(1), 67–74. doi:10.1007/s11596-019-2001-y [PubMed: 30868493]
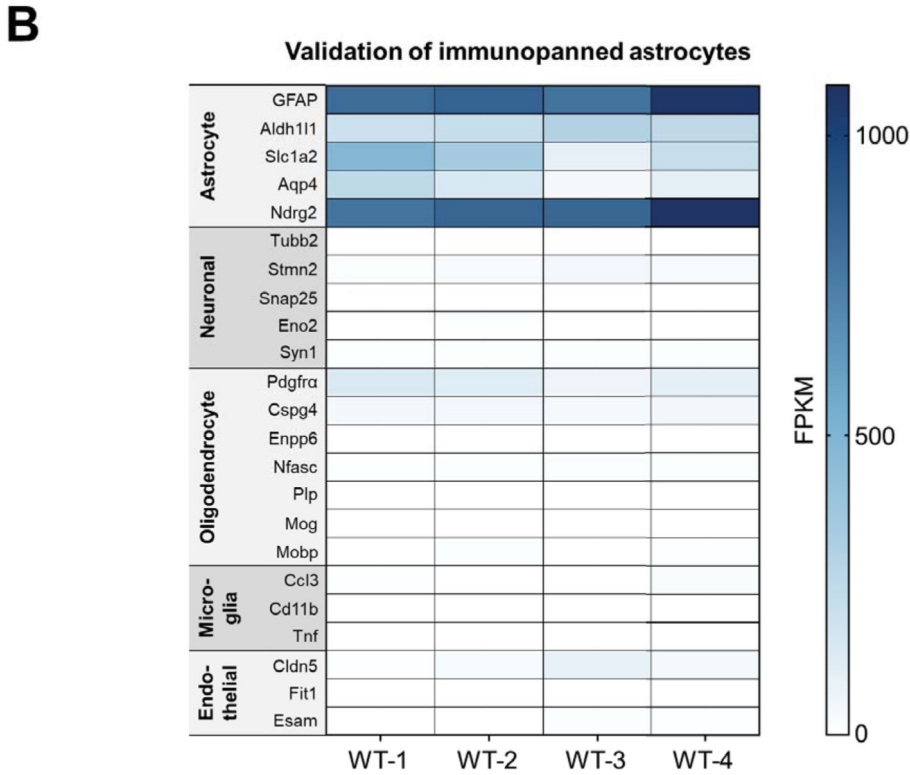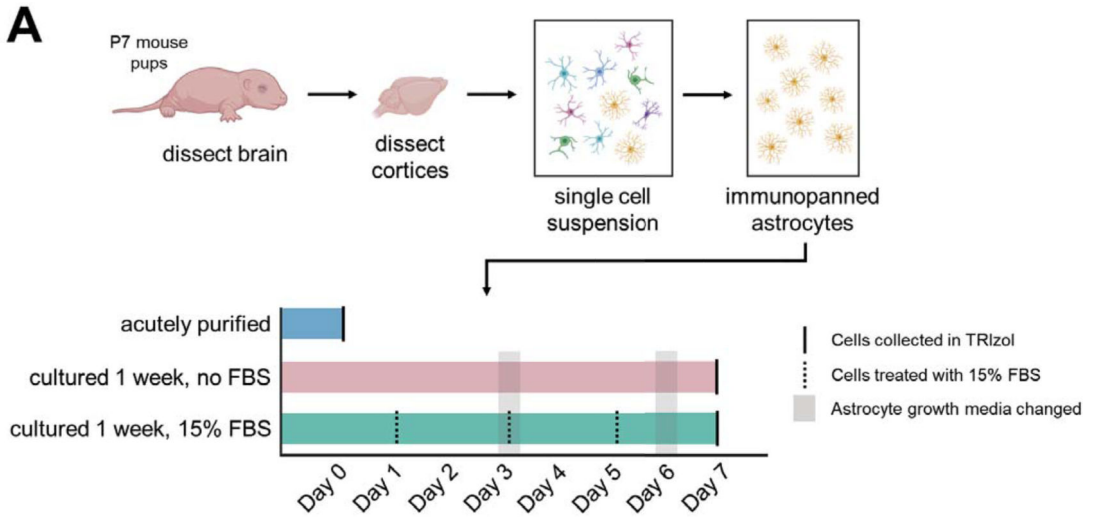
Figure 1. Experimental design and validation of purity of immunopanned astrocytes.
(A) A schematic outlining the experimental design of the different conditions that were made as samples for RNA-seq analysis. Astrocytes were immunopanned from P7 WT and L1KO mouse pups and used for 3 different conditions: 1) no treatment, no culturing (acute), 2) cultured for 1 week, no treatment, and 3) cultured for 1 week, but treated with 15% FBS every other day. The acutely purified astrocytes were collected immediately in TRIzol and RNA was isolated for RNA-seq analysis. For cultured astrocytes, astrocytes were cultured for 1 week with half media changes every 3 days. For cultured astrocytes treated with 15%

FBS, cells were treated with 15% FBS every other day for 1 week. At the end of the week, all astrocytes were collected in TRIzol and RNA was isolated for RNA-seq analysis. (B) To validate the purity of the immunopanned astrocytes used in RNA-seq analyses, FPKM values for WT acutely immunopanned astrocyte samples (n=4) were obtained for selected cell-specific gene markers from our RNA-seq data. From four samples of WT immunopanned astrocytes, there was high expression of astrocyte-specific genes such as GFAP and NDRG2. In contrast, there were extremely low levels of oligodendrocyte and endothelial cell contamination as evidenced by low expression of oligodendrocyte-specific and endothelial-specific genes.
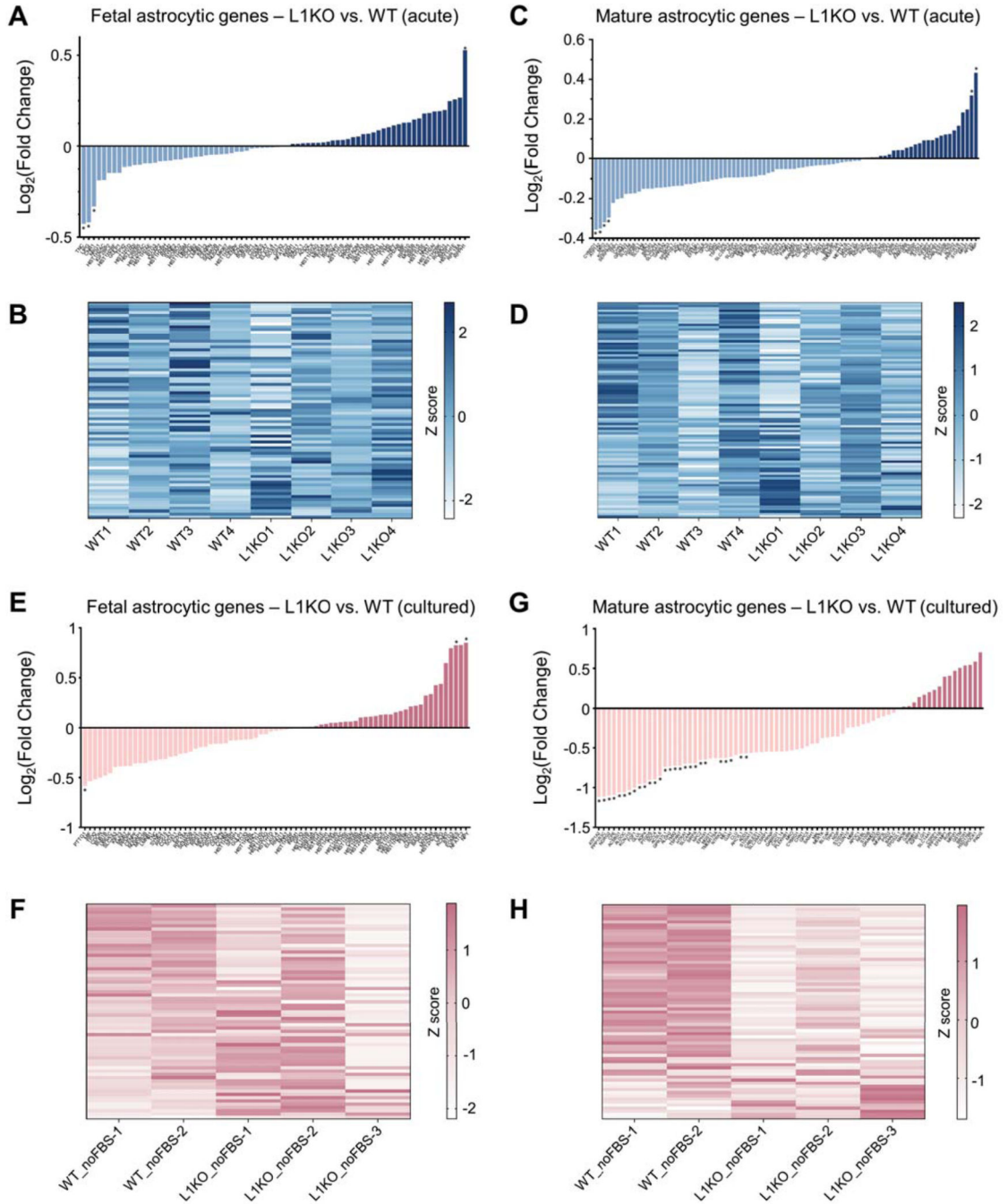
Figure 2. Changes in fetal and mature astrocytic genes in acutely immunopanned astrocytes and 1-week-cultured astrocytes from P7 L1KO mouse brains compared to WT mouse brains.
Log$_2$(Fold Change) values from our RNA-seq analysis were assessed against a published list of 100 fetal astrocytic genes (Sloan et al., 2017). The graphs in panels A-D represent data from acutely immunopanned astrocytes, whereas the graphs in panels E-H represent data from 1-week-cultured, untreated immunopanned astrocytes. (A) Only 4 fetal astrocytic genes were found to be significantly downregulated (TNC, LIPG, CNR1, and GPR37L1, which is not shown here) with only one fetal astrocytic gene significantly upregulated (RPPH1). The rest of the fetal astrocytic genes were not found to be significantly changed

between L1KO and WT acutely immunopanned astrocytes. (B) Heat map of Z scores of the corresponding 100 fetal astrocytic genes of individual samples used in RNA-seq analysis. (C) Only 4 mature astrocytic genes (CYBRD1, ATP1A2, MRO, and KCNJ10) were found to be significantly downregulated and 2 mature astrocytic genes (APOD and MBP) were found to be significantly upregulated. The rest of the mature astrocytic genes were not found to be significantly changed between L1KO and WT acutely immunopanned astrocytes. (D) Heat map of Z scores of the corresponding 100 mature astrocytic genes of individual samples used in RNA-seq analysis. (E) Only one gene (PPTG1) was found to be significantly downregulated and two genes (EOMES and NPY) were found to be significantly upregulated. The rest of the genes were not found to be significantly different between L1KO immunopanned astrocytes vs. WT immunopanned astrocytes after 1 week in culture. (F) Corresponding heat map showing the gene expression of the 100 fetal astrocytic genes of the individual WT and L1KO samples. (G) A large number of mature astrocytic genes were found to be significantly downregulated (ATP1A2, PPP1R3C, NDRG2, CPE, ACSBG1, ALDOC, KCNJ10, FGF1, GLUL, AQP4, PTGDS, SDC4, ACSL6, GPR37L1, ALDH2, TMX2, TSPAN7, HTRA1, SLC4A4, SIRPA, NPC2, EPHX1, NTRK, ME1, GJA1, AHCYL1, and ADD3) in L1KO astrocytes compared to WT astrocytes, with none being significantly upregulated. (H) Corresponding heat map showing gene expression of 100 mature astrocytic genes of the individual WT and L1KO samples. WT=wild-type; L1KO=GPR37L1 knockout; *p value 0.05
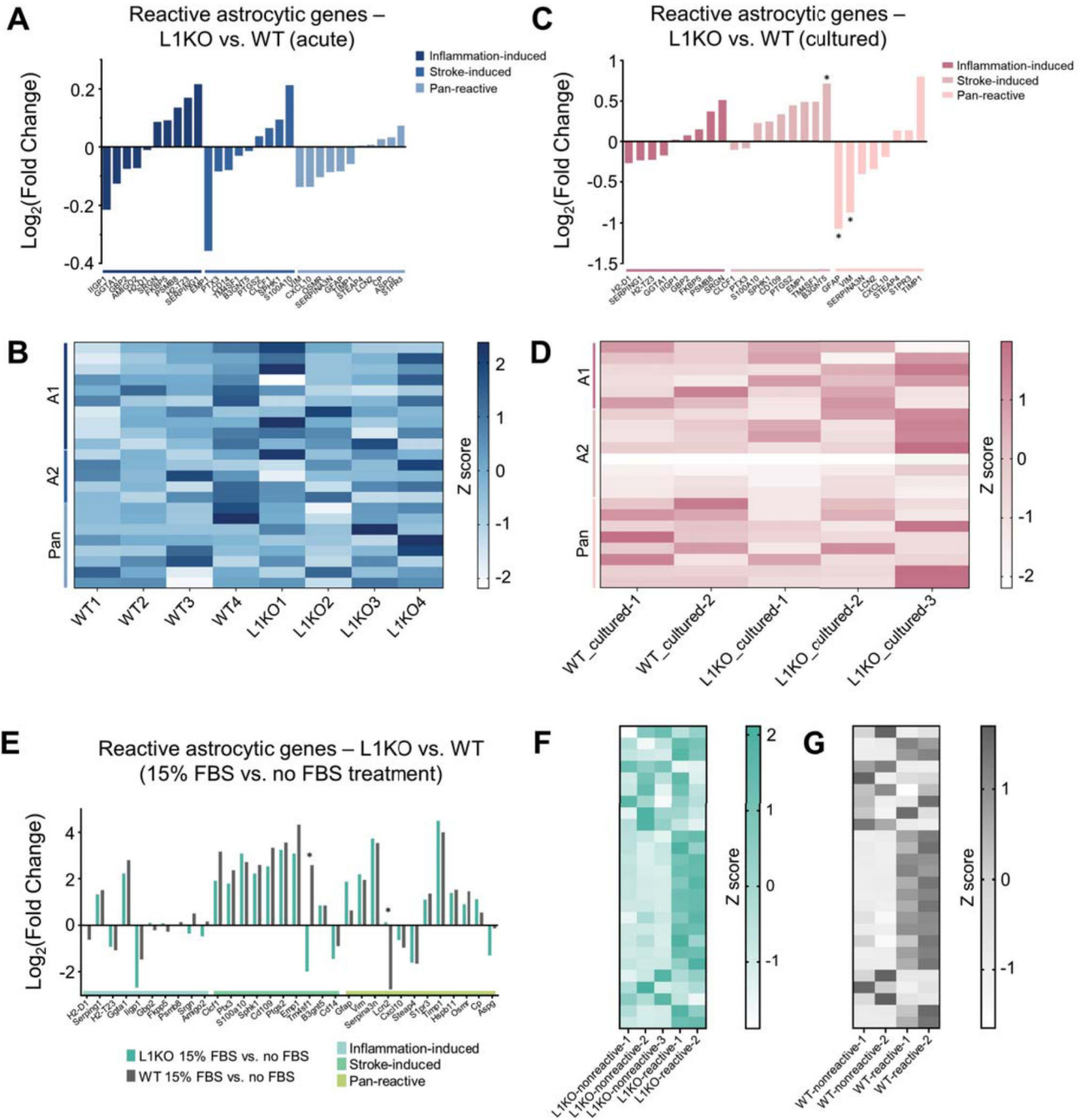
Figure 3. Loss of GPR37L1 does not lead to increased astrocyte reactivity.

Log$_2$(Fold Change) values from our RNA-seq analyses were assessed against a published list of 38 reactive astrocytic genes (Liddelow et al., 2017). The graphs shown in panels A and B represent expression of reactive astrocytic genes in acutely immunopanned astrocytes, whereas the graphs shown in panels C and D represent expression of reactive astrocytic genes in 1-week-cultured, untreated immunopanned astrocytes and the graphs shown in panels E and F represent expression of reactive astrocytic genes of 1-week-cultured astrocytes treated with 15% FBS. (A) Log$_2$(Fold Change) values reveal that no reactive

astrocytic genes from three subtypes of astrocyte reactivity were significantly changed between L1KO and WT acutely immunopanned astrocytes at P7. (B) Corresponding heat map of Z scores of the 38 reactive astrocytic genes of individual samples used in RNA-seq analysis. (C) After 1 week in culture, only 3 reactive astrocytic genes were found to be significantly changed in L1KO immunopanned astrocytes compared to WT (B3GNT5, GFAP, and VIM). However, all other reactive genes were not significantly changed. (D) Corresponding heat map of Z scores of the 38 reactive astrocytic genes of individual samples used in RNA-seq analysis. (E) Log_2(Fold Change) values of genes from L1KO and WT immunopanned astrocytes that were cultured for 1 week and treated with 15% FBS to induce pan-reactivity normalized to gene expression from 1-week-cultured but untreated immunopanned astrocytes. For each genotype, differential expression analysis was performed to assess Log_2(Fold Change) values between the 15% FBS-treated condition and non-treated condition to establish a normalized Log_2(Fold Change) value. WT and L1KO values were then graphed next to each other to see how fold gene changes compared to each other. Only TM4SF1 and LCN2 were found to be significantly different between WT and L1KO astrocytes (Student's T-test for each gene, p value 0.05). (F-G) Corresponding heat maps of individual WT and L1KO astrocyte samples. WT=wild-type; L1KO=GPR37L1 knockout; *p value 0.05 for differences between WT and L1KO values
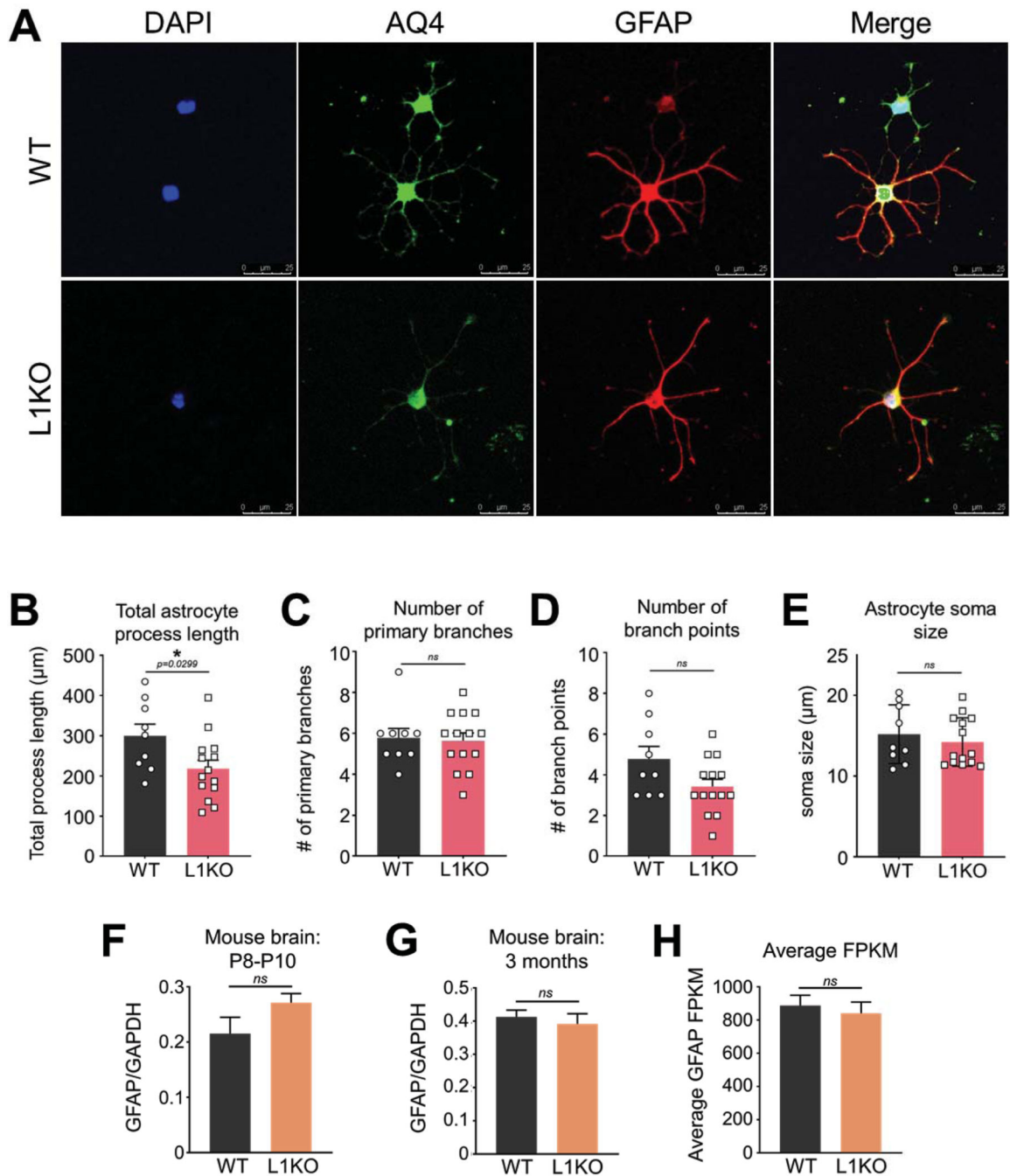
Figure 4. Cortical astrocytes lacking GPR37L1 have shorter total process length compared to WT astrocytes.

Cortical astrocytes were immunopanned from P7 L1KO and WT mice and plated, fixed and stained once astrocyte projections were visible (1 day after immunopanning). (A) Representative images of wild-type (WT) and GPR371-knockout (L1KO) astrocytes. (B) Quantification of astrocyte total process length. (C) Quantification of number of primary branches. (D) Quantification of number of number of branch points. (E) Quantification of astrocyte soma size (diameter). Statistical analyses were performed via Student's T-test between the two genotypes; bars represent SEM (n=9 for WT and n=14 for L1KO). (F)

Quantification of GFAP protein expression levels in P8-P10 WT and L1KO mouse brain lysates. (G) Quantification of GFAP protein expression levels in 3-month-old WT and L1KO mouse brain lysates. (H) Average FPKM values of GFAP in WT and L1KO astrocytes immunopanned from P7 animals. Student's t-test; bars represent SEM (n=4 per genotype).
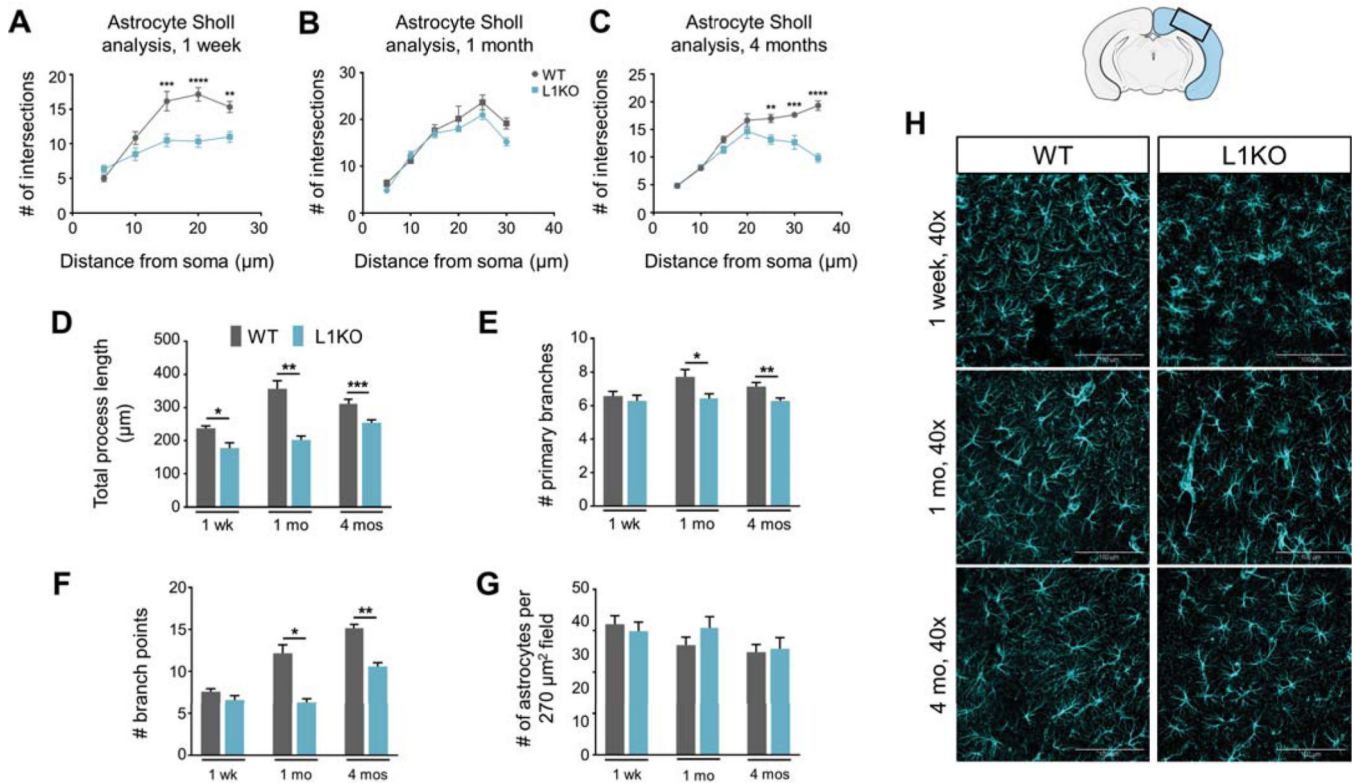
Figure 5. Morphological analyses of L1KO astrocytes compared to WT astrocytes reveal loss of astrocyte complexity at later developmental timepoints.

Sholl analysis and quantifications of total astrocyte length, number of primary branches, and number of branch points were performed in order to quantify morphological differences between L1KO and WT cortical astrocytes in the mouse brain at 1 week, 1 month, and 4 months of age. (A-C) Sholl analysis (two-way ANOVA with Sidak's correction for multiple comparisons) of WT and L1KO astrocytes in mouse brain from (A) 1-week-old (n=6 per genotype; **p value=0.0063, ***p value=0.0002, ****p value<0.0001), (B) 1-month-old (n=5 for WT, n=6 for L1KO), and (C) 4-month-old mice (n=6 per genotype, **p value=0.0084, ***p value=0.0003, ****p value<0.0001). (D-G) Quantifications of astrocyte morphology in WT and L1KO astrocytes in mouse cortex (n=7 per genotype per timepoint, two-tailed Student's T-test), (D) Total process length (*p value=0.0049, **p value<0.0001, ***p value=0.0046), (E) Number of primary branches (*p value=0.0288, **p value=0.0134), (F) Number of branch points (*p value=0.0002,**p value<0.0001), (G) number of astrocytes per 270μm^2 field. (H) Representative images of GFAP-stained astrocytes in the WT and L1KO mouse cortex. All bars shown in this figure represent SEM.
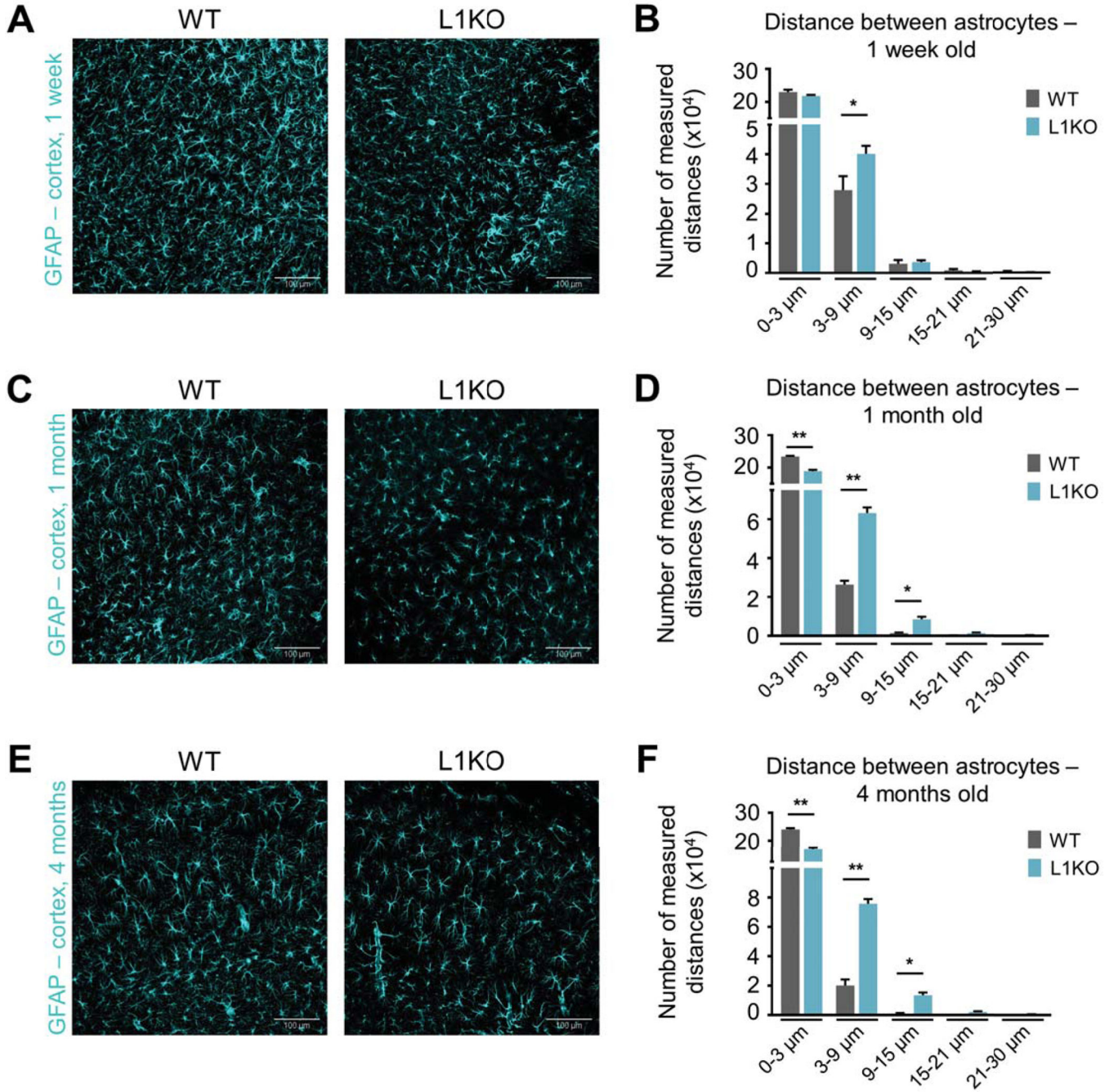
Figure 6. Loss of GPR37L1 leads to sparser astrocytic spacing in the mouse cortex.
Cortical brain sections from WT and L1KO mice were stained with the astrocytic marker GFAP and distance mapping was calculated for astrocytes in the mouse cortex. Representative images and quantifications are shown for astrocytes from 1-week-old mice (panels A and B), 1-month-old mice (panels C and D), and 4-month-old mice (panels E and F). (B) Quantified distances between astrocytic surfaces for astrocytes from 1-week-old mice (*p value=0.0225, n=10 per genotype). Quantification revealed that L1KO astrocytes were spaced slightly further apart from each other compared to WT astrocytes, with a

significant number of measured distances in the 3–9 μm range. (D) Quantified distances between astrocytic surfaces for astrocytes from 1-month-old mice (*p value=0.0464, **p value<0.0001; n=9 for WT, n=8 for L1KO). At 1 month, L1KO astrocytes were spaced significantly further apart from each other compared to WT astrocytes, with significant differences in the first three distance bins. (F) Quantified distances between astrocytic surfaces for astrocytes from 4-month-old mice (*p value=0.0117, **p value<0.0001; n=10 for WT, n=9 for L1KO). At 4 months, significant differences were again observed between WT and L1KO astrocytic spacing in the first three distance bins. All graphs were analyzed via two-way ANOVA with Sidak's correction for multiple comparisons. All bars represent SEM.
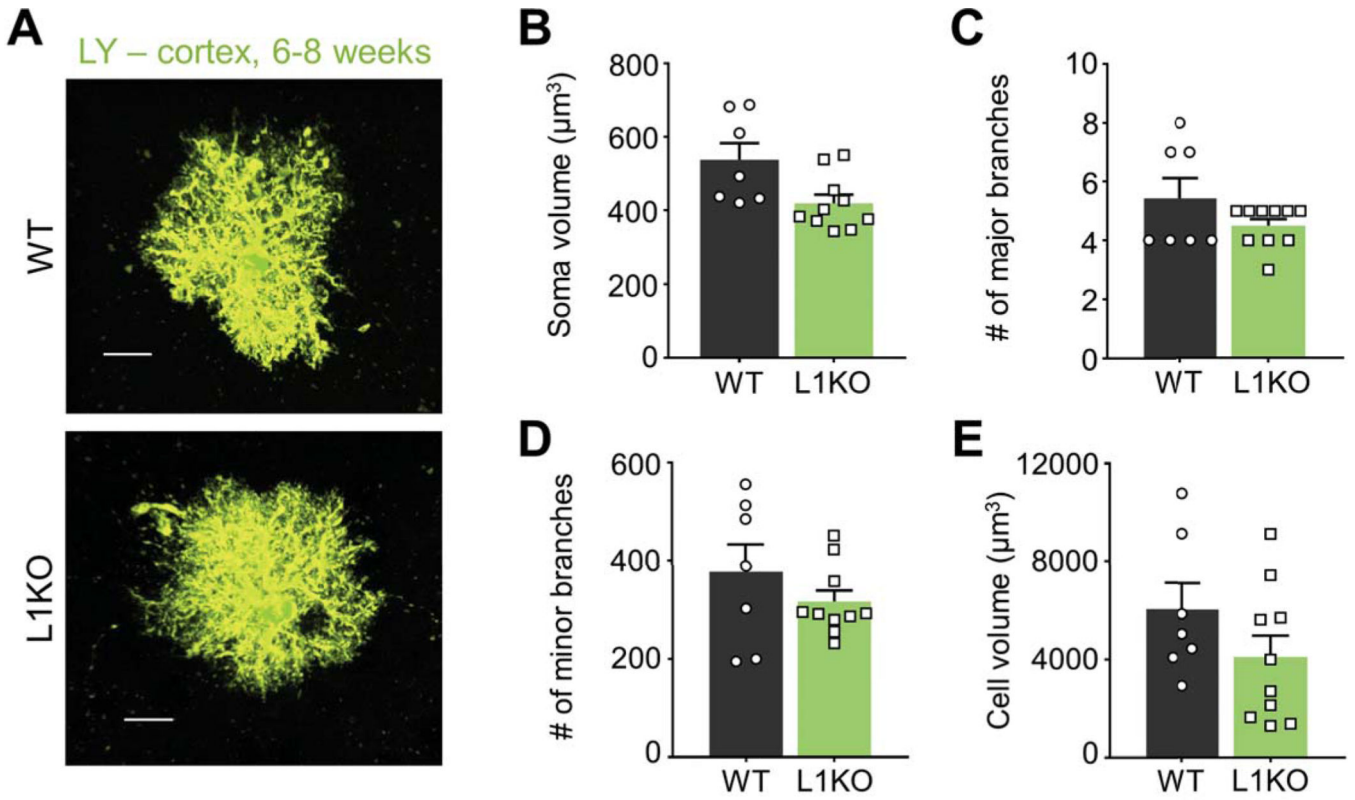
Figure 7. Cell volume is not significantly different between WT and L1KO astrocytes at 6–8 weeks.

Brain sections from WT and L1KO mouse brains (6–8 weeks old, n=7 for WT, n=10 for L1KO) were fixed, astrocytes in the cortex were identified and backfilled with Lucifer Yellow to visualize fine distal processes, and morphological features were quantified via IMARIS. (A) Representative images of WT and L1KO backfilled astrocytes. Scale bars are 10μm. (B) Soma volume (μm^3) was not significantly different between WT and L1KO astrocytes. (C) Number of major branches was not significantly different between WT and L1KO astrocytes. (D) Numbers of minor branches were not significantly different between WT and L1KO astrocytes. (E) Total cell volume (μm^3) was not significantly different between WT and L1KO astrocytes. All bars this figure represent SEM.

Table 1.

Top 50 most significantly downregulated genes in acutely immunopanned astrocytes from P7 GPR37L1 knockout mice vs. wild-type mice

Gene name	Log2 Fold Change	Fold Change	% change	p value
Gpr37l1	−3.099761376	−4.28638	−94.88%	1.14E-86
Snhg6	−1.297761715	−1.22924	−57.35%	1.55E-25
D2hgdh	−1.079453009	−1.05662	−51.92%	7.92E-13
Colgalt2	−0.827875061	−0.88753	−45.95%	1.03E-09
Gm10516	−0.819946985	−0.88267	−45.76%	3.01E-07
Lmod1	−0.800397088	−0.87079	−45.32%	6.08E-07
Ugt1a6a	−0.749067048	−0.84035	−44.15%	3.22E-06
Ube2t	−0.709268416	−0.81749	−43.26%	2.27E-06
Ddr2	−0.69268496	−0.80814	−42.89%	7.95E-06
Nav1	−0.664530859	−0.79253	−42.27%	1.39E-05
Gpr55	−0.660579758	−0.79036	−42.18%	3.80E-05
Ackr1	−0.658539997	−0.78924	−42.14%	3.20E-06
Adhfe1	−0.628463548	−0.77296	−41.48%	3.87E-05
Rab7b	−0.574955714	−0.74482	−40.33%	0.00024
Gm7694	−0.572179882	−0.74338	−40.27%	1.01E-05
Pla2g3	−0.558743707	−0.73649	−39.98%	0.000347
Rgs7	−0.528810647	−0.72137	−39.35%	0.001048
4933400C23Rik	−0.514481372	−0.71424	−39.05%	0.00142
Ccdc115	−0.510162808	−0.71211	−38.96%	0.000149
Cd44	−0.509294803	−0.71168	−38.94%	0.000199
Snord58b	−0.506764783	−0.71043	−38.89%	7.70E-05
3110045C21Rik	−0.498610564	−0.70643	−38.72%	0.00094
Ankrd55	−0.463108809	−0.68925	−37.98%	0.00391
Lamc1	−0.455774848	−0.68576	−37.83%	0.000503
Tmem163	−0.452683398	−0.68429	−37.77%	0.004616
Nuf2	−0.448629507	−0.68237	−37.69%	0.005216
Dusp23	−0.446580491	−0.6814	−37.64%	0.005648
Hmgb1	−0.442519331	−0.67949	−37.56%	0.005604
Efhd1	−0.440087118	−0.67834	−37.51%	0.001757
Msx2	−0.429843521	−0.67354	−37.30%	0.005402
Copa	−0.428045024	−0.6727	−37.27%	0.001116
6720483E21Rik	−0.427975737	−0.67267	−37.27%	0.002313
Tnc	−0.42635077	−0.67192	−37.23%	0.006895
Ppox	−0.4217972	−0.6698	−37.14%	0.000509
Vangl2	−0.421779958	−0.66979	−37.14%	0.003687
Lipg	−0.417940588	−0.66801	−37.06%	0.009102
Gm3704	−0.41352323	−0.66597	−36.97%	0.010408
Rpl17	−0.412345781	−0.66542	−36.95%	0.00942

Gene name	Log2 Fold Change	Fold Change	% change	p value
Casq1	−0.409801768	−0.66425	−36.90%	0.01066
Magel2	−0.405263652	−0.66217	−36.81%	0.012054
Gm960	−0.397940267	−0.65881	−36.66%	0.013077
Spata3	−0.397924753	−0.65881	−36.66%	0.011682
Ppic	−0.392858324	−0.6565	−36.56%	0.001751
Fgfbp3	−0.390422375	−0.65539	−36.51%	0.010152
Tcam1	−0.389812313	−0.65511	−36.50%	0.009607
Tram2	−0.388828721	−0.65466	−36.48%	0.012485
Rrs1	−0.387082931	−0.65387	−36.44%	0.007588
Hdhd2	−0.383661163	−0.65232	−36.37%	0.001639
Kcnj9	−0.381051151	−0.65115	−36.32%	0.017614
Fam84a	−0.381033159	−0.65114	−36.32%	0.011712

Log_2 Fold Changes were calculated via DESeq2 and the top 50 most significantly (p 0.05) downregulated genes are listed in ascending order.

Table 2.

Top 50 most significantly upregulated genes in acutely immunopanned astrocytes from P7 GPR37L1 knockout mice vs. wild-type mice

Gene name	Log2 Fold Change	Fold Change	% change	p value
Clec3b	1.823053084	1.769146	240.85%	8.81E-30
Prss56	0.865825502	0.911191	88.06%	5.47E-08
Wdfy1	0.841171282	0.895752	86.06%	1.87E-07
Chil1	0.767044048	0.85089	80.36%	6.40E-07
Adamts4	0.680955617	0.801601	74.30%	1.36E-05
3110009E18Rik	0.669515927	0.79527	73.54%	2.01E-06
Mag	0.653511443	0.786496	72.49%	5.15E-05
Fam129a	0.638902892	0.778572	71.54%	6.76E-05
Tmem37	0.588563142	0.751874	68.40%	0.000266
Pm20d1	0.568264314	0.741369	67.18%	0.000296
Sgk2	0.568032657	0.74125	67.16%	0.000211
Ndn	0.561021667	0.737657	66.75%	0.00013
Gm9994	0.553944982	0.734047	66.33%	4.71E-06
Cldn11	0.551177244	0.73264	66.17%	0.000624
Adat2	0.551146259	0.732625	66.17%	2.78E-05
Rpph1	0.529046912	0.721488	64.89%	0.000856
Xcr1	0.518722336	0.716343	64.30%	2.87E-05
S1pr5	0.515328085	0.71466	64.11%	0.001324
Cdcp1	0.494206428	0.704273	62.93%	6.11E-05
Ppp1r14a	0.493174991	0.70377	62.88%	0.001922
Nell1	0.490526521	0.702479	62.73%	0.00234
9930012K11Rik	0.485286948	0.699932	62.44%	0.002452
Neu4	0.479684735	0.697219	62.14%	0.002946
Msc	0.469107745	0.692127	61.57%	0.003645
3110079O15Rik	0.46663848	0.690943	61.43%	0.003593
Kcne4	0.453553535	0.684705	60.74%	0.0027
Pigz	0.439646127	0.678136	60.01%	0.006177
Mbp	0.4329903	0.675014	59.66%	0.005603
Cdhr1	0.430437984	0.673821	59.53%	0.007189
Bend6	0.430331656	0.673772	59.52%	0.007652
Cpm	0.42314416	0.670423	59.15%	0.007915
St8sia5	0.416985251	0.667567	58.84%	0.007844
Gjb1	0.412188209	0.665351	58.60%	0.006799
Rab4a	0.404185671	0.661671	58.19%	0.007099
Slc14a2	0.387727763	0.654166	57.37%	0.015992
Gng4	0.382577028	0.651834	57.12%	0.017091
Slc5a11	0.382174846	0.651653	57.10%	0.017324
Gabre	0.380188273	0.650756	57.00%	0.018364

Gene name	Log2 Fold Change	Fold Change	% change	p value
Gm10638	0.379914013	0.650632	56.99%	0.018541
Creg2	0.379775646	0.65057	56.98%	0.017899
Thbs4	0.377875764	0.649714	56.89%	0.01923
Pdlim2	0.375069345	0.648451	56.75%	0.017495
C130050O18Rik	0.374905845	0.648377	56.74%	0.00998
Mog	0.372234576	0.647178	56.61%	0.009477
Gjc2	0.36983848	0.646104	56.49%	0.014549
Gsn	0.369699127	0.646042	56.49%	0.011153
Akr1c13	0.367497297	0.645056	56.38%	0.021687
Th	0.367006279	0.644837	56.36%	0.009523
Gpr176	0.366562583	0.644639	56.33%	0.019076
Cldn2	0.364184507	0.643577	56.22%	0.023141

Log_2 Fold Changes were calculated via DESeq2 and the top 50 most significantly (p 0.05) upregulated genes are listed in descending order.

Table 3.

Top 50 most significantly downregulated genes in immunopanned astrocytes from P7 GPR37L1 knockout mice vs. wild-type mice, 1 week in culture, no FBS

Gene name	Log2 Fold Change	Fold Change	% change	p value
Lcn2	−1.950861311	−1.93302636	−73.81%	1.73E-06
Trf	−1.355657965	−1.27956902	−58.81%	4.51E-05
Thrsp	−1.348621142	−1.27334305	−58.63%	0.000224
Car3	−1.317094194	−1.24581875	−57.83%	0.000108
Lpo	−1.276472769	−1.21122994	−56.81%	0.00028
Rpl37a	−1.268458901	−1.20452046	−56.61%	0.000737
Hmgb1	−1.226272472	−1.16980858	−55.55%	0.00088
Gpd1	−1.216729373	−1.1620961	−55.31%	5.72E-05
Cacng5	−1.203879791	−1.15179167	−54.99%	0.000377
Rnf145	−1.183567378	−1.13568865	−54.49%	0.00051
Dbp	−1.179469839	−1.13246765	−54.39%	0.000458
Kcnip3	−1.162236751	−1.11902072	−53.96%	0.000236
Zhx3	−1.160978577	−1.11804525	−53.93%	6.10E-05
Rab26	−1.149387209	−1.10909828	−53.64%	0.000439
Sft2d1	−1.146337288	−1.10675607	−53.57%	0.001352
Nudt21	−1.145842943	−1.1063769	−53.55%	0.000213
Lpin3	−1.143577789	−1.10464116	−53.50%	5.52E-05
Aldh1a1	−1.13465997	−1.09783403	−53.28%	0.002795
Atp1a2	−1.116755279	−1.08429347	−52.84%	1.18E-05
Ppp1r3c	−1.112882809	−1.08138692	−52.74%	0.00046
Sparcl1	−1.111802858	−1.08057773	−52.72%	2.17E-05
Sdhc	−1.105461272	−1.07583831	−52.56%	0.000261
Ndrg2	−1.09684627	−1.06943313	−52.35%	4.75E-05
Cpe	−1.090621006	−1.06482844	−52.20%	7.01E-05
Grm3	−1.089437418	−1.06395521	−52.17%	0.000232
Ache	−1.089435997	−1.063954162	−52.17%	0.001004923
Cspg5	−1.089079642	−1.063691391	−52.16%	0.00024979
Shisa4	−1.086149374	−1.061533112	−52.09%	0.000357837
Abat	−1.083173639	−1.059345827	−52.02%	0.00010563
Myo6	−1.07389384	−1.0525537	−51.79%	6.07E-05
Cp	−1.073076922	−1.051957867	−51.77%	9.22E-05
Il34	−1.07024285	−1.049893398	−51.70%	0.001492499
Tjp1	−1.068164197	−1.048381788	−51.65%	0.000103745
Gdpd2	−1.066675214	−1.047300328	−51.61%	0.000385095
Cxx1c	−1.065484021	−1.046435958	−51.58%	0.003227086
Fam84a	−1.062467855	−1.044250515	−51.51%	0.000102232
Acsbg1	−1.05962706	−1.042196316	−51.44%	0.00106709
Mcee	−1.056797653	−1.040154368	−51.37%	0.007600356

Gene name	Log2 Fold Change	Fold Change	% change	p value
Aldoc	−1.055281123	−1.039061555	−51.34%	0.002578155
Chst7	−1.055015584	−1.038870325	−51.33%	0.001669805
A2m	−1.049038975	−1.03457553	−51.18%	0.0001602
Dio2	−1.045198941	−1.031825454	−51.09%	0.000227331
Snrpg	−1.044679087	−1.031453717	−51.08%	0.013443487
Gm2115	−1.03871358	−1.027197488	−50.93%	0.001788948
Kcnj10	−1.029254668	−1.020484782	−50.70%	0.003051223
Slc6a11	−1.028214575	−1.019749341	−50.68%	0.000355359
Gbp3	−1.024158881	−1.016886654	−50.58%	0.00402988
Hadhb	−1.022743836	−1.015889746	−50.55%	0.003200463
Rps16	−1.021871115	−1.015275396	−50.53%	0.021148278
Mapk4	−1.018777297	−1.0131005	−50.45%	0.000405167

Log_2 Fold Changes were calculated via DESeq2 and the top 50 most significantly (p 0.05) downregulated genes are listed in ascending order.

Table 4.

Top 50 most significantly upregulated genes in immunopanned astrocytes from P7 GPR37L1 knockout mice vs. wild-type mice, 1 week in culture, no FBS

Gene name	Log2 Fold Change	Fold Change	% change	p value
Lars2	3.666783	6.350115	8057.84%	2.46E-30
Mir682	3.664845	6.341594	8009.80%	6.86E-21
Mir6236	3.343631	5.075784	3272.59%	3.63E-26
Ifi202b	2.625564	3.085629	748.92%	9.83E-11
Alb	2.116947	2.168875	349.67%	2.12E-10
Gm5088	2.013775	2.019188	305.36%	2.59E-06
Rbp4	1.965019	1.952089	286.93%	1.96E-06
Gdf7	1.891055	1.854532	261.63%	1.39E-05
Gm4737	1.796234	1.736562	233.24%	3.85E-05
P2rx1	1.642449	1.560977	195.05%	0.000125
Gm19782	1.6368	1.554877	193.81%	0.000134
Foxl1	1.604844	1.520814	186.95%	0.000162
Olfr893	1.582438	1.497378	182.33%	0.000284
Pzp	1.573535	1.488165	180.53%	1.44E-05
Ttr	1.568368	1.482845	179.50%	0.000128
Itln1	1.559569	1.473829	177.76%	0.000179
Pck1	1.54046	1.454436	174.05%	8.73E-05
Tcl1	1.523352	1.437291	170.81%	0.000539
Cyp3a11	1.52121	1.435158	170.41%	0.000165
Ces3a	1.511182	1.425217	168.55%	0.000411
Wdr86	1.50916	1.423222	168.18%	0.00052
Lrriq4	1.503453	1.417603	167.14%	0.000425
Gc	1.50337	1.417521	167.13%	0.000107
G6b	1.49108	1.405497	164.91%	0.000533
Gm5801	1.477499	1.392328	162.50%	0.000824
Gcnt3	1.474407	1.389347	161.96%	0.000286
Ccl9	1.471816	1.386854	161.51%	0.000678
Gm3434	1.459904	1.37545	159.45%	0.000879
Stxbp3-ps	1.443265	1.359678	156.63%	0.00112
Ankrd60	1.430534	1.347732	154.51%	0.00125
Ace3	1.42725	1.344668	153.97%	0.000483
Hoxa13	1.426428	1.343902	153.84%	0.001068
Ahsg	1.424132	1.341765	153.46%	0.000453
Gata5	1.421612	1.339423	153.05%	0.000764
Cyp4a10	1.419756	1.337702	152.75%	0.000479
Olfr1010	1.404486	1.323618	150.29%	0.001352
Gm10637	1.393505	1.313581	148.56%	0.001652
Gpr34	1.38993	1.31033	148.00%	0.001514

Gene name	Log2 Fold Change	Fold Change	% change	p value
Slamf9	1.389058	1.309538	147.86%	0.00096
Ccl24	1.386433	1.307158	147.45%	0.001741
C6	1.380511	1.301803	146.54%	0.001195
Nxph4	1.374507	1.296396	145.61%	0.001881
Galp	1.373299	1.295312	145.43%	0.001862
Cyp2e1	1.362176	1.285363	143.74%	0.0011
Afp	1.361313	1.284595	143.61%	0.000327
Fga	1.351083	1.275518	142.09%	0.000232
Rdh9	1.350964	1.275412	142.07%	0.001826
Vmn1r233	1.348868	1.273561	141.76%	0.002325
Ldhc	1.345741	1.270803	141.30%	0.002394
Ildr1	1.344308	1.269542	141.08%	0.001157

Log_2 Fold Changes were calculated via DESeq2 and the top 50 most significantly (p 0.05) upregulated genes are listed in ascending order.